WILEY

Investigation and elimination of nonlinear Poisson stiffening in 3d and solid shell finite elements

Tobias Willmann[ORCID] | **Simon Bieber** | **Manfred Bischoff**

Institute for Structural Mechanics, University of Stuttgart, Stuttgart, Germany

Correspondence
Tobias Willmann, Institute for Structural Mechanics, University of Stuttgart, Pfaffenwaldring 7, 70550 Stuttgart, Germany.
Email: willmann@ibb.uni-stuttgart.de

Abstract

We show that most geometrically nonlinear three-dimensional shell elements and solid shell elements suffer from a previously unknown artificial stiffening effect that only appears in geometrically nonlinear problems, in particular in the presence of large bending deformations. It can be interpreted as a nonlinear variant of the well-known Poisson thickness locking effect. We explain why and under which circumstances this phenomenon appears and propose concepts to avoid it.

KEYWORDS

3d-shells, locking, nonlinear, solid shells, stiffening effect

1 | INTRODUCTION

Three-dimensional shell finite elements are a well-established means for the numerical simulation of thin-walled structures. They can be based on a discretization of the midsurface, like classical shell elements, or as solid shell elements with nodes at the top and bottom surface of the shell body. Certain members of the first group are often denoted as 7-parameter shell elements, because they use seven degrees of freedom (DOFs) to describe the three-dimensional shell kinematics.

In the following, we use the term "3d-shell elements" to refer to both versions. Many different 3d-shell elements for geometrically nonlinear problems have been proposed in the literature and most of them share two properties: they are formulated based on Green–Lagrange strains and one parameter, namely the seventh DOF, is introduced to enhance the transverse normal strain such that it becomes a linear function of the thickness coordinate in order to avoid so-called Poisson thickness locking. This additional strain component is introduced either via the enhanced assumed strain (EAS) method,[1] for example, in References 2 and 3, via a quadratic displacement field in thickness direction, for example, in References 4 and 5, to name only some of the earliest works. Furthermore, the DOFs for the description of the thickness change and the quadratic displacement field can be condensed on element level, see for example Reference 6. Recently, new 3d-shell elements have been presented, for example, a corotational formulation in Reference 7 and a formulation based on the assumed natural inhomogeneous strain approach in combination with 21 EAS

parameters in Reference 8. Regarding the elimination of Poisson thickness locking, they use the same methods mentioned above.

In the past decade, the isogeometric analysis has experienced increasing popularity. Consequently, isogeometric 3d-shell elements have been developed, for example, References 9 and 10. An isogeometric Timoshenko beam with extensible directors has been presented in Reference 11, which uses the EAS method to alleviate Poisson locking. This approach is similar to the elimination of Poisson thickness locking in a 3d-shell element. The isogeometric formulations avoid Poisson thickness locking either by using a quadratic displacement field in thickness direction or by using the EAS method, that is, they use the same methods as formulations based on Lagrangian shape functions.

Following the definition of Reference 12 we relate the term "locking" to the appearance of parameter-dependent reduced convergence rates in the pre-asymptotic range. Thus, the symptoms of locking vanish in case of an infinitely fine mesh in all spatial directions. However, using surface-oriented shell elements, Poisson thickness locking does not vanish with mesh refinement since the mesh can, by definition, only be refined in the shell plane. Therefore, we avoid the term locking and rather denote this phenomenon as a "stiffening effect" that is caused by a deficit in the corresponding shell model. On the other hand, one may argue that for solid shell elements, mesh refinement in thickness direction is possible (although usually not desired), which would justify to call Poisson thickness locking a locking effect. The same is true for the geometrically nonlinear version of this phenomenon, presented in this contribution. As our results are relevant for both midsurface based 3d-shell elements and solid shell elements and we want to emphasize the appearance in geometrically linear and nonlinear formulations, we decide to use "linear Poisson stiffening effect" (LPS) for what is called Poisson thickness locking in the literature and we use "nonlinear Poisson stiffening effect" (NPS) for the new stiffening effect described in this article.

In a geometrically linear 3d-shell element formulation, the additional linear strain component in transverse direction is sufficient to avoid LPS. However, for large bending strains, for example, in the simulation of sheet metal forming processes, an overly stiff response was observed in Reference 13, which deteriorates the simulation results immensely. To the authors' best knowledge to date, this artificial stiffening effect has not been understood and explained in the literature. The observed artificial stiffening effect depends on Poisson's ratio and solely occurs in geometrically nonlinear element formulations. It can be regarded as LPS, extended to nonlinear problems. We show that most of the geometrically nonlinear 3d-shell elements based on the Green–Lagrange strain suffer from NPS, since a linear transverse normal strain component is not sufficient to avoid it. Furthermore, NPS is not restricted to Green–Lagrange strain and might appear as well for other strain measures. Additionally, solutions how to avoid NPS are proposed.

This research was triggered while studying methods for modeling and simulation of sheet metal forming problems, where it is common to use five, seven, or nine integration points in thickness direction rather than two integration points, which is sufficient for purely elastic analysis. The number of integration points plays a crucial role for the observed nonlinear stiffening effect. From several possible ways to investigate stiffening effects, we choose to conduct an analysis of constraints for isochoric deformations at integration points to identify parasitic strain.

This contribution is organized as follows. In Section 2, we derive conditions that 3d-shell elements need to fulfill in order to be able to represent an isochoric deformation correctly and use elastic material models for both small and large strain as a starting point. In Section 3, we define a generic 3d-shell element and show its inability to fulfill the conditions derived in Section 2 for geometrically nonlinear problems under certain circumstances. Furthermore, we explain how element formulations need to be enhanced such that they can represent isochoric deformations correctly and therefore do not suffer from NPS. In Section 4, we perform a bending test with the 3d-shell elements presented in References 14 and 15 as well as several modifications of these elements to underline the theoretical derivations from Section 3.

2 | ISOCHORIC CONDITIONS IN DIFFERENT KINEMATIC SETTINGS

Poisson stiffening affects a finite element solution when material behavior with a sufficiently large Poisson's ratio is considered. Such material behavior typically occurs in elastic rubber-like materials or metals described by elasto-plastic material models. Three different material models will be considered in this article: Hooke's law (Hooke), the St. Venant-Kirchhoff material model (SVK) and a compressible Neo-Hookean material model (NH). Expressed with bulk

Abbreviation	$\mathcal{W}_{vol}$ depends on	Exemplary material model	Typically associated with
trε	tr ε	Hooke's law	geom. linear, small strains
trE	tr $\mathbf{E}$	St. Venant-Kirchhoff	geom. nonlin., small strains
detF	$J = \det \mathbf{F}$	Neo-Hooke	geom. nonlin., large strains

modulus K and shear modulus μ, the corresponding strain energy density functions are given by

$$\mathcal{W}^{\text{Hooke}}(\varepsilon) = \underbrace{\frac{K}{2}(\text{tr } \varepsilon)^2}_{\mathcal{W}^{\text{Hooke}}_{\text{vol}}} + \underbrace{2\mu\left(\text{tr } \varepsilon^2 - \frac{1}{6}(\text{tr } \varepsilon)^2\right)}_{\mathcal{W}^{\text{Hooke}}_{\text{dev}}}, \tag{1a}$$

$$\mathcal{W}^{\text{SVK}}(\mathbf{E}) = \underbrace{\frac{K}{2}(\text{tr } \mathbf{E})^2}_{\mathcal{W}^{\text{SVK}}_{\text{vol}}} + \underbrace{2\mu\left(\text{tr } \mathbf{E}^2 - \frac{1}{6}(\text{tr } \mathbf{E})^2\right)}_{\mathcal{W}^{\text{SVK}}_{\text{dev}}}, \tag{1b}$$

$$\mathcal{W}^{\text{NH}}(\mathbf{E}) = \underbrace{\frac{K}{2}\left(\log J\right)^2}_{\mathcal{W}^{\text{NH}}_{\text{vol}}} + \underbrace{\frac{\mu}{2}\left(I_1 - 3 - 2\log J - \frac{2}{3}\left(\log J\right)^2\right)}_{\mathcal{W}^{\text{NH}}_{\text{dev}}}. \tag{1c}$$

Here, the displacement gradient $\mathbf{H} = \frac{\partial \mathbf{u}}{\partial \mathbf{X}}$ can be used to define the linear strain tensor and the Green–Lagrange strain tensor as

$$\varepsilon = \frac{1}{2}\left(\mathbf{H} + \mathbf{H}^{\text{T}}\right), \qquad \mathbf{E} = \frac{1}{2}\left(\mathbf{H} + \mathbf{H}^{\text{T}} + \mathbf{H}^{\text{T}}\mathbf{H}\right). \tag{2}$$

Furthermore, we define the two invariants

$$J = \det \mathbf{F} = \sqrt{\det \mathbf{C}} = \sqrt{\det(2\mathbf{E} + \mathbf{I})}, \qquad I_1 = \text{tr } \mathbf{C} = \text{tr}(2\mathbf{E} + \mathbf{I}), \tag{3}$$

with the deformation gradient $\mathbf{F} = \mathbf{1} + \mathbf{H}$ and the right Cauchy–Green strain tensor $\mathbf{C} = \mathbf{F}^{\text{T}}\mathbf{F}$. Different strain energy functions for Neo-Hookean material models can be found in the literature. A detailed discussion of the Neo-Hookean strain energy function shown above can be found in Reference 16. The derivations that follow are also valid for the frequently used Neo-Hooke form

$$\mathcal{W} = \frac{\mu}{2}(I_1 - 3) - \mu \log J + \frac{\Lambda}{4}\left(J^2 - 1 - 2\log J\right). \tag{4}$$

We assume the material to be homogeneous, that is, the parameters of each material model are assumed to be constant within the entire shell body.

Each strain energy function is split into a volumetric and a deviatoric part. As we investigate Poisson stiffening effects, our focus lies on the volumetric part, more precisely, on the question on which strain measure or deformation measure the volumetric part depends. The strain energy functions (1) represent three groups of material models, which are summarized in Table 1.

The table reads as follows: the "trε" case means we assume that the volumetric part of the used strain energy function depends on tr ε. A typical use case for such material models is a geometrically linear simulation based on the assumption of small strain.

Let $\mathbf{u}^{\text{iso}}$ be an isochoric deformation. For such deformations, the volumetric part of the strain energy function has to vanish. Regarding the different dependencies of $\mathcal{W}_{vol}$, this requires

$$\text{tr } \varepsilon = r_{\text{tr}\varepsilon} \overset{!}{=} 0, \tag{5a}$$

$$tr\,\mathbf{E} = r_{\text{trE}} \overset{!}{=} 0, \tag{5b}$$

$$\sqrt{\det\left(2\mathbf{E} + \mathbf{I}\right)} - 1 \overset{!}{=} 0. \tag{5c}$$

Condition (5c) is true if and only if

$$\det\mathbf{C} = \det\left(2\mathbf{E} + \mathbf{I}\right) = r_{\text{detF}} \overset{!}{=} 1. \tag{6}$$

Throughout this article, we refer to the conditions stated in (5a), (5b), and (6) as "isochoric conditions", which are fulfilled in the continuous case, but not necessarily in a discrete setting. In case these conditions are not satisfied, we use the residuals r from (5a), (5b), and (6) for further investigation. The strain energy function for an isochoric displacement $\mathbf{u}^{\text{iso}}$ yields

$$\mathcal{W}\left(\mathbf{u}^{\text{iso}}\right) = \mathcal{W}_{\text{dev}}\left(\mathbf{u}^{\text{iso}}\right) = c < \infty. \tag{7}$$

In particular, c is independent of the bulk modulus K.

Poisson stiffening is related to the inability to correctly represent an isochoric deformation, such that

$$\lim_{K \to \infty} \mathcal{W}\left(\varepsilon^h\right) = \infty \qquad \text{or} \qquad \lim_{K \to \infty} \mathcal{W}\left(\mathbf{E}^h\right) = \infty, \tag{8}$$

holds. Here ε^h and $\mathbf{E}^h$ are the approximated strain tensors provided by a finite element. Physically, this means that the amount of energy required to impose $\mathbf{u}^{\text{iso}}$ artificially increases with increasing bulk modulus. Furthermore, the resulting artificial stresses increase.

An element suffers from Poisson stiffening if it is unable to satisfy the isochoric conditions at all integration points simultaneously. Let us consider ε^h and assume that it does not fulfill condition (5a), that is, $r_{\text{tr}\varepsilon} \neq 0$ in the incompressible limit for at least one integration point. This results in

$$\lim_{K \to \infty} \mathcal{W}\left(\varepsilon^h\right) = \lim_{K \to \infty}\left(\mathcal{W}_{\text{vol}}\left(\varepsilon^h\right) + \mathcal{W}_{\text{dev}}\left(\varepsilon^h\right)\right) = \lim_{K \to \infty}\left(\frac{K}{2}r_{\text{tr}\varepsilon}^2 + \mathcal{W}_{\text{dev}}\left(\varepsilon^h\right)\right) = \infty, \tag{9}$$

because both $r_{\text{tr}\varepsilon}$ and $\mathcal{W}_{\text{dev}}$ do not depend on K. This equation holds for $\mathbf{E}^h$ as well. Therefore, the isochoric conditions are necessary conditions to be fulfilled by an element in order to be free from Poisson stiffening. Besides the correct asymptotic behavior in the incompressible limit, from an engineering perspective the question is whether the violation of these conditions influences simulation results for a given bulk modulus. Therefore, the residuals r will be analyzed in the next section.

For further investigation we transform the conditions (5a), (5b), and (6) and express them as a requirement on the transverse normal strain component:

$$\varepsilon_{33} \overset{!}{=} -\varepsilon_{11} - \varepsilon_{22}, \qquad (\text{tr}\varepsilon) \tag{10a}$$

$$E_{33} \overset{!}{=} -E_{11} - E_{22}, \qquad (\text{tr}E) \tag{10b}$$

$$E_{33} \overset{!}{=} \frac{1 - M_{3,3}(\mathbf{C}) + 4E_{13}^2\left(1 + 2E_{22}\right) + 4E_{23}^2\left(1 + 2E_{11}\right) - 16E_{12}E_{13}E_{23}}{2M_{3,3}(\mathbf{C})}. \qquad (\text{detF}) \tag{10c}$$

$M_{3,3}(\mathbf{C})$ denotes the minor of $\mathbf{C}$ obtained by eliminating the third row and column:

$$M_{3,3}(\mathbf{C}) = \det\begin{bmatrix} C_{11} & C_{12} \\ C_{21} & C_{22} \end{bmatrix}. \tag{11}$$

The derivation of Equation (10c) can be found in Appendix A.

In the following sections, we show that 3d-shell elements are usually able to fulfill the isochoric condition in the trε case (10a), but most of them are not able to satisfy the isochoric conditions in the trE case (10b) and the detF case

(10c). This is shown in theoretical derivations and numerical examples. Furthermore, a solution is provided how 3d-shell elements can be enhanced to satisfy equations (10b) and to reduce the error in (10c).

3 | ARTIFICIAL VOLUMETRIC STIFFENING IN VARIOUS KINEMATIC SETUPS

3.1 | General problem statement—Geometrically linear

Within this section, all variables refer to discretized quantities and we therefore omit the superscript h for the sake of better readability. For the subsequent explanations we employ the natural coordinates (ξ, η, ζ), where (ξ, η) denote the in-plane coordinates and ζ denotes the coordinate in thickness direction, as shown in Figure 1. The global coordinate system with directions 1, 2, and 3 is identical to the natural coordinate system. As usual, ξ, η, ζ are in the range $[-1, 1]$.

We first define a generic 6-parameter shell element, for the time being omitting the aforementioned 7th parameter that introduces a linear variation of the transverse normal strain and thus removes LPS. It can be formulated as an 8-node solid shell element (SolS) with three DOFs at each node and an interpolation using Lagrange shape functions, that is,

$$\mathbf{u}^{\text{SolS}}(\xi, \eta, \zeta) = \sum_{i=1}^{8} N_i^{\text{tri}}(\xi, \eta, \zeta)\, \mathbf{d}_i, \tag{12}$$

with the trilinear Lagrange shape functions $N_i^{\text{tri}}(\xi, \eta, \zeta)$ and the displacement DOFs $\mathbf{d}_i$ at each node:
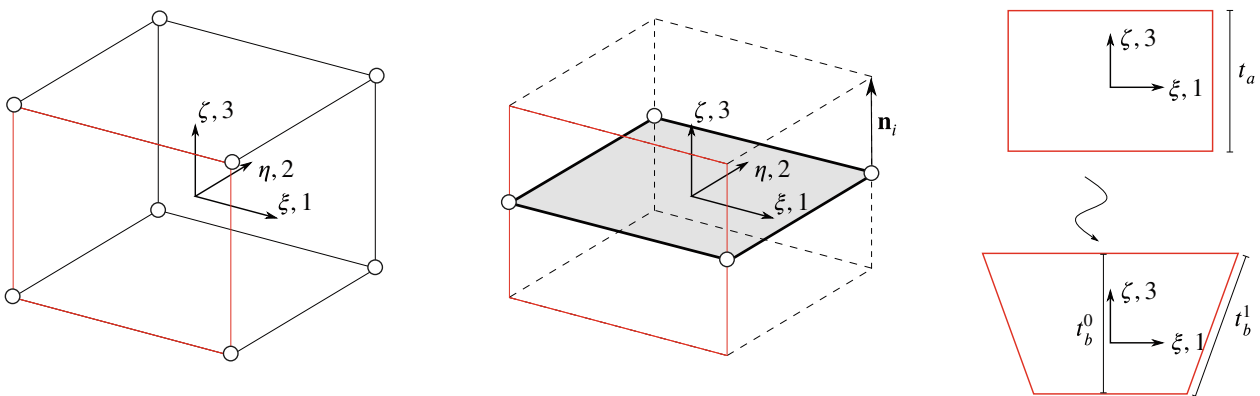
$$N_i^{\text{tri}}(\xi, \eta, \zeta) = \frac{1}{8}(1 \pm \xi)(1 \pm \eta)(1 \pm \zeta), \qquad \mathbf{d}_i = \begin{bmatrix} d_x^i & d_y^i & d_z^i \end{bmatrix}^{\mathrm{T}}. \tag{13}$$

Throughout this article, we consider the case of only one single layer of solid shell elements through the thickness. Then, the element can be equivalently formulated as a 4-node midsurface based shell element (MidS) with six DOFs per node, three displacements and three components of the nodal director, that is

$$\mathbf{u}^{\text{MidS}}(\xi, \eta, \zeta) = \sum_{i=1}^{4} \left(N_i^{\text{bi}}(\xi, \eta)\, \mathbf{d}_i + \zeta N_i^{\text{bi}}(\xi, \eta)\, \Delta\mathbf{n}_i \right), \tag{14}$$

with the bilinear shape functions $N_i^{\text{bi}}(\xi, \eta)$ and the change of the nodal director $\Delta\mathbf{n}_i$:

$$N_i^{\text{bi}}(\xi, \eta) = \frac{1}{4}(1 \pm \xi)(1 \pm \eta), \qquad \Delta\mathbf{n}_i = \begin{bmatrix} \Delta n_x^i & \Delta n_y^i & \Delta n_z^i \end{bmatrix}^{\mathrm{T}}. \tag{15}$$

FIGURE 1 Sketch of the generic 3d-shell element as a solid shell element (left), as a midsurface based shell element (center) and the applied deformation projected onto the ξ-ζ-plane (right). The indicated lengths (t_a, t_b) are referred to later in the context of the geometrically nonlinear case.

In Figure 1 the volume of the midsurface based shell element is sketched with dashed lines, its midsurface is drawn in grey and a nodal director $\mathbf{n}_i$ is indicated at one node. Both formulations result in an identical displacement field, that is,

$$\mathbf{u}^{\text{SolS}}(\xi, \eta, \zeta) \equiv \mathbf{u}^{\text{MidS}}(\xi, \eta, \zeta). \tag{16}$$

As a model problem for the subsequent analyses we consider a bending-like displacement field of the form

$$u_1 = k_1 \xi \zeta, \tag{17a}$$
$$u_2 = 0, \tag{17b}$$
$$u_3 = k_3 \zeta. \tag{17c}$$

The displacement in η-direction is constrained, which results in a plane strain condition in the ξ-ζ-plane. This simplifies the subsequent analysis without loss of generality. k_1 is a prescribed value within the range $k_1 \in (-1, 1), k_1 \neq 0$ and k_3 is a free parameter, that is, we allow the element to change its thickness during deformation.

Figure 1 (right) shows the element deformation projected to the ξ-ζ-plane.

To avoid rank deficiency of the stiffness matrix, at least two integration points are necessary in ζ-direction. Using more than two integration points might look like an artificial problem setup for the elastic problems discussed in this article, but it is highly relevant in other almost incompressible problem setups, for example, elasto-plastic sheet metal forming operations (see for instance Reference 17).

3.2 | Linear Poisson stiffening effect (LPS)— trε case

3.2.1 | Analysis of the effect

Although the reasons for LPS are well-known, we repeat it in this section as a basis for the extension to the nonlinear regime. The applied deformation (17) yields the following diagonal entries to the geometrically linear strain tensor:

$$\varepsilon_{11}^{\text{u}} = k_1 \zeta, \tag{18a}$$
$$\varepsilon_{22}^{\text{u}} = 0, \tag{18b}$$
$$\varepsilon_{33}^{\text{u}} = k_3. \tag{18c}$$

Here, superscript u marks the displacement based strain (also sometimes called compatible strain). As only these strain components are necessary for fulfillment of Equation (10a), the remaining strain components are not shown. It can be easily seen that this formulation does not satisfy (10a) at two or more locations $\zeta \in [-1, 1]$ simultaneously, for instance at two integration points, since

$$k_3 \neq -k_1 \zeta. \tag{19}$$

Thus, this primal element suffers from LPS.

For comparison with the later described NPS, we deduce an upper bound for the absolute value of the residual $r_{\text{tr}\varepsilon}$ defined in (5a). For the primal element formulation discussed so far, this is

$$|r_{\text{tr}\varepsilon}| = |k_3 + k_1 \zeta| \leq |k_3| + |k_1 \zeta|. \tag{20}$$

This bound depends on the free parameter k_3. For $k_3 = 0$ the upper bound of the residual in (20) is minimized and the estimate becomes

$$|r_{\text{tr}\varepsilon}^{\text{opt}}| \leq |k_1 \zeta|. \tag{21}$$

3.2.2 | Methods to avoid LPS

To resolve the well known LPS problem, the generic 6-parameter shell element needs to be enhanced to a generic 7-parameter shell element, in which $\varepsilon_{33}^{\text{u}}$ is linear in ζ. This can be accomplished either using the EAS method or by adding

a quadratic displacement field to u_3. Without loss of generality, we use the EAS method for this type of enhancement throughout this article. The total strain tensor of the generic 7-parameter shell element can then be written as

$$\varepsilon = \varepsilon^u + \tilde{\varepsilon}^1. \tag{22}$$

The strain tensor enhancement

$$\tilde{\varepsilon}^1 = \begin{bmatrix} \tilde{\varepsilon}_{11} & \tilde{\varepsilon}_{22} & \tilde{\varepsilon}_{33} & 2\tilde{\varepsilon}_{12} & 2\tilde{\varepsilon}_{23} & 2\tilde{\varepsilon}_{13} \end{bmatrix}^T = \mathbf{B}_e^1 \boldsymbol{\alpha}^1, \tag{23}$$

can be written as a product of the enhanced strain displacement operator and the vector of EAS parameters

$$\mathbf{B}_e^1 = \begin{bmatrix} 0 & 0 & \zeta & 0 & 0 & 0 \end{bmatrix}^T, \qquad \boldsymbol{\alpha}^1 = \begin{bmatrix} \alpha_1 \end{bmatrix}. \tag{24}$$

The superscript "1" indicates the number of EAS parameters used. With Equation (22) the strain in thickness direction becomes

$$\varepsilon_{33} = k_3 + \alpha_1 \zeta. \tag{25}$$

The trace of the strain tensor then reads

$$\mathrm{tr}\,\varepsilon = k_3 + k_1 \zeta + \alpha_1 \zeta, \tag{26}$$

and the isochoric condition (10a) becomes

$$k_3 + \alpha_1 \zeta \overset{!}{=} -k_1 \zeta. \tag{27}$$

Due to the additional EAS parameter, for every $\zeta \in [-1, 1]$ there exists a solution for k_3 and α_1 that fulfills (27). Thus, the generic 7-parameter shell element is free from LPS.

Almost every 3d-shell element available in the literature includes an enhancement of the transverse normal strain such that it is linear w.r.t. the thickness coordinate, either via EAS or via a quadratic displacement field, see References 1-5. In the subsequent three sections, we extend the discussion of Poisson stiffening to the geometrically nonlinear cases trE and detF. We show that the enhancement from Equation (23) is not sufficient to avoid Poisson stiffening in the geometrically nonlinear cases.

3.3 | General problem statement—Geometrically nonlinear

Similar to the geometrically linear case, we define a generic 3d-shell element for the geometrically nonlinear cases. Regarding DOFs, shape functions and applied displacement we use the setup from in Section 3.1. Green–Lagrange strain is used as nonlinear strain measure. The displacement-based Green–Lagrange strain tensor $\mathbf{E}^u$ is split into constant, linear and quadratic parts in ζ:

$$\mathbf{E}^u(\xi, \eta, \zeta) = \mathbf{E}_0(\xi, \eta) + \zeta \mathbf{E}_1(\xi, \eta) + \zeta^2 \mathbf{E}_2(\xi, \eta). \tag{28}$$

We define two different element formulations.

In the first one, all three terms are included, as it is done in most of the literature on solid-shell elements. In the second one, marked with superscript "red" for "reduced", the quadratic contributions with respect to ζ are neglected,

$$\mathbf{E}^{u,\mathrm{red}}(\xi, \eta, \zeta) = \mathbf{E}_0(\xi, \eta) + \zeta \mathbf{E}_1(\xi, \eta). \tag{29}$$

Depending on the problem solved, there might be a notable difference between the standard and reduced formulation. An example that investigates this difference is provided in fig. 18 of Reference 15. As we will see later, the two formulations also have different properties regarding NPS.
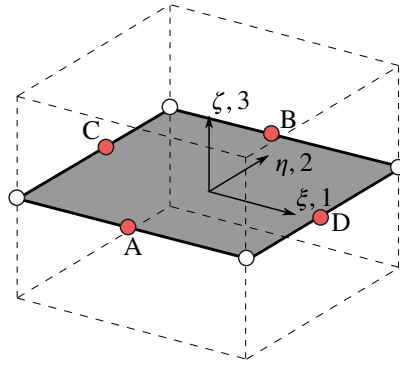
FIGURE 2 Collocation points (A–D) for the ANS method to prevent transverse shear locking. E_{13} is collocated at A and B, E_{23} is collocated at C and D, linear interpolation is used in between.

In the analysis of Poisson stiffening in the geometrically linear case, there is no need to consider shear strain components because they do not appear in the isochoric condition (10a). In contrast to this, in the geometrically nonlinear regime they do appear in the isochoric condition (10c). Therefore, a calculation of the shear strain components is necessary and shear locking has to be taken into account. We apply the assumed natural strain (ANS) method[18] to avoid transverse shear locking. It is used for both $\mathbf{E}^{u}$ and $\mathbf{E}^{u,red}$, with the collocation points shown in Figure 2. Furthermore, as we have seen in Section 3.2 for the geometrically linear case, it is necessary to enhance the transverse normal strain to avoid LPS. This is typically done in geometrically nonlinear 3d-shell element available in the literature, see for instance References 2,3,15,17, and 19. We use the EAS method for both the standard and the reduced formulation, which yields

$$\mathbf{E}^{1} = \mathbf{E}^{u} + \tilde{\mathbf{E}}^{1}, \qquad \mathbf{E}^{red} = \mathbf{E}^{u,red} + \tilde{\mathbf{E}}^{red,1} \tag{30}$$

with

$$\tilde{\mathbf{E}}^{1} = \tilde{\mathbf{E}}^{red,1} = \begin{bmatrix} \tilde{E}_{11} & \tilde{E}_{22} & \tilde{E}_{33} & 2\tilde{E}_{12} & 2\tilde{E}_{23} & 2\tilde{E}_{13} \end{bmatrix}^{T} = \mathbf{B}_{e}^{1}\boldsymbol{\alpha}^{1} \tag{31}$$

with the same $\mathbf{B}_{e}^{1}$ and $\boldsymbol{\alpha}^{1}$ as in Equation (24). Again, superscript "1" indicates the number of EAS parameters used.

3.4 | Nonlinear Poisson stiffening effect (NPS)—trE case

3.4.1 | Analysis of the effect

Applying the displacement field given in (17), the diagonal entries of the enhanced Green–Lagrange strain tensor for the standard element formulation are

$$E_{11}^{1} = k_{1}\zeta + \frac{1}{2}k_{1}^{2}\zeta^{2}, \tag{32a}$$

$$E_{22}^{1} = 0, \tag{32b}$$

$$E_{33}^{1} = \underbrace{k_{3} + \frac{1}{2}k_{3}^{2}}_{\text{const.}} + \underbrace{\frac{1}{2}k_{1}^{2}\xi^{2}}_{\text{fiber elongation}} + \underbrace{\alpha_{1}\zeta}_{\text{enhanced strain}}. \tag{32c}$$

The transverse normal strain component in Equation (32c) can be split into three different contributions: a part which is constant throughout the element, the enhanced strain, which comes along with the seventh parameter α_{1} and a contribution associated with an elongation of transverse fibers. The latter is a geometrically nonlinear effect and it is also indicated in Figure 1. The length change of the fiber in the center of the element $t_{b}^{0} - t_{a}$ is different from the length change of the fiber at the element edge, $t_{b}^{1} - t_{a}$. Therefore, this contribution depends on ξ.

We define the abbreviation $c = k_3 + \frac{1}{2}k_3^2 + \frac{1}{2}k_1^2\xi^2$ as the sum of the constant contribution and the contribution from transverse fiber elongation in (32c). Thus, the transverse normal strain component can be written in compact form as

$$E_{33}^1 = c + \alpha_1\zeta. \tag{33}$$

As c contains the free parameter k_3, c itself can be regarded as a free parameter. The calculation of the strain tensors for the standard and reduced element formulation along with applying the ANS method result in

$$\mathbf{E}^1 = \begin{bmatrix} k_1\zeta + \frac{1}{2}k_1^2\zeta^2 & 0 & 0 \\ 0 & 0 & 0 \\ 0 & 0 & c + \alpha_1\zeta \end{bmatrix}, \qquad \mathbf{E}^{\mathrm{red},1} = \begin{bmatrix} k_1\zeta & 0 & 0 \\ 0 & 0 & 0 \\ 0 & 0 & c + \alpha_1\zeta \end{bmatrix}. \tag{34}$$

The detailed calculation of these tensors can be found in Appendix B. As we investigate the trE case, the generic 3d-shell element needs to satisfy condition (10b). For the standard formulation (34)$_1$ this condition reads

$$c + \alpha_1\zeta \overset{!}{=} -k_1\zeta - \frac{1}{2}k_1^2\zeta^2. \tag{35}$$

It cannot be satisfied for every $\zeta \in [-1, 1]$ due to the quadratic term ζ^2 on the right-hand side. This argument is formally similar to the one that explains LPS from the inability of the primal element formulation to satisfy (19) in the linear case in Section 3.2.

Similar to (21) we can derive an upper bound for the absolute value of r_{trE}:

$$|r_{\mathrm{trE}}| = \left| c + (k_1 + \alpha_1)\zeta + \frac{1}{2}k_1^2\zeta^2 \right| \le |c| + |(k_1 + \alpha_1)\zeta| + \left| \frac{1}{2}k_1^2\zeta^2 \right|. \tag{36}$$

Again, the upper bound depends on the free parameters, in this case α_1 and c. Analogously to (21), we investigate the optimal case and choose the free parameters such that they minimize the upper bound, that is, $c = 0$ and $\alpha_1 = -k_1$. This yields

$$|r_{\mathrm{trE}}^{\mathrm{opt}}| \le \left| \frac{1}{2}k_1^2\zeta^2 \right|. \tag{37}$$

So far, while discussing condition (35) we have not yet considered the fact that numerical quadrature is used in ζ-direction. In fact, the condition must only hold at the integration points and its violation in between has no effect on the numerical solution. For $N_{\mathrm{GP}}^\zeta = 2$ the condition can be interpreted as a polynomial interpolation problem: Find c, α_1 such that $c + \alpha_1\zeta_i = -k_1\zeta_i - \frac{1}{2}k_1^2\zeta_i^2$ for all N_{GP}^ζ integration point locations ζ_i. This problem has a unique solution for $N_{\mathrm{GP}}^\zeta = 2$, that is, c and α_1 can take values such that (35) is fulfilled at two integration points. Thus, in the frequently applied case of using two integration points through the thickness, there is no NPS. If $N_{\mathrm{GP}}^\zeta \ge 3$, the element suffers from NPS. Equation (35) cannot be fulfilled at three or more integration points simultaneously, because no corresponding solution for the polynomial interpolation problem exists. In these cases, the elements suffer from NPS.

Because $N_{\mathrm{GP}}^\zeta = 2$ integration points are not enough to capture the higher order terms in geometrically nonlinear analysis, it can also be interpreted as reduced integration or underintegration. This is a popular concept to avoid locking and thus this interpretation provides a nice analogy to the reason while no NPS occurs when using $N_{\mathrm{GP}}^\zeta = 2$.

NPS does not depend on the number of integration points in the shell plane $\left(N_{\mathrm{GP}}^\xi, N_{\mathrm{GP}}^\eta\right)$. NPS appears for both full integration $\left(N_{\mathrm{GP}}^\xi = 2, N_{\mathrm{GP}}^\eta = 2\right)$ and reduced integration $\left(N_{\mathrm{GP}}^\xi = 1, N_{\mathrm{GP}}^\eta = 1\right)$. It does not diminish with h-refinement or p-refinement.

The influence of NPS on the solution is less severe than the influence of LPS for equal Poisson's ratio and equal magnitude of strain. A comparison of the optimal case residuals (21) and (37) shows that $\left|r_{\mathrm{trE}}^{\mathrm{opt}}\right|$ (NPS) is smaller than $\left|r_{\mathrm{treps}}^{\mathrm{opt}}\right|$ (LPS), because both $|\zeta_i|$ and $|k_1|$ are smaller than or equal to 1. Let us recall that both estimates are derived based on the assumption that the free parameters minimize the residual, which is not necessarily true. Nevertheless, from the authors' point of view, the comparison of the optimal case estimates justifies the expectation that the influence of NPS on the solution is less severe than the influence of LPS.

In contrast to the standard element formulation, the reduced element formulation $(34)_2$, which excludes the quadratic part of the strain tensor does not suffer from NPS, because the isochoric condition for $\mathbf{E}^{\mathrm{red},1}$ is $c + \alpha_1 \zeta \overset{!}{=} k_1 \zeta$, similar to the geometrically linear case. The part of the strain tensor being quadratically dependent on ζ that causes NPS for the standard formulation is not present in the reduced formulation.

In summary, the following observations can be made for the trE case:

- The reduced formulation is always free from NPS.
- Whether or not NPS occurs in the standard formulation, depends on the number of Gauss points N_{GP}^{ζ} in ζ-direction.
- If $N_{\mathrm{GP}}^{\zeta} = 2$, the standard element is free from NPS.
- If $N_{\mathrm{GP}}^{\zeta} \geq 3$, the standard element suffers from NPS.

3.4.2 | Methods to avoid NPS in the trE case

In the following, we present a method to avoid NPS in the trE case. For the standard element formulation, the strain tensor of the element has to be modified such that its trace can be equal to zero for $N_{\mathrm{GP}}^{\zeta} \geq 3$. A possible solution is to introduce an additional EAS parameter that adds the missing quadratic term in ζ. The resulting formulation can be interpreted as an 8-parameter shell model with two parameters introduced via EAS, analogously to 7-parameter shell elements where the seventh parameter is often introduced via EAS. In both cases, the enhanced strain field is discontinuous at element borders.

The enhanced strain tensor $\tilde{\mathbf{E}}^2$ of the generic 8-parameter shell element can be written as

$$\tilde{\mathbf{E}}^2 = \mathbf{B}_e^2 \boldsymbol{\alpha}^2 \tag{38}$$

with

$$\mathbf{B}_e^2 = \begin{bmatrix} 0 & 0 & \zeta & 0 & 0 & 0 \\ 0 & 0 & L_2(\zeta) & 0 & 0 & 0 \end{bmatrix}^{\mathrm{T}}, \qquad \boldsymbol{\alpha}^2 = \begin{bmatrix} \alpha_1 & \alpha_2 \end{bmatrix}^{\mathrm{T}}, \qquad L_2(\zeta) = \frac{1}{2}\left(3\zeta^2 - 1\right), \tag{39}$$

where L_2 is the second Legendre polynomial in ζ-direction. A quadratic strain enhancement for solid elements with the ansatz $(39)_3$ was already investigated in Reference 20. It was shown that the initial stiffness matrix is not affected by these modes, that is, the same stiffness matrices as for standard EAS elements are obtained. However, in contrast to the present study, the influence of geometrical nonlinearities was not considered.

Additional enhancements of the transverse normal strain, like $\xi L_2(\zeta)$, may be sensible, but they are not considered here, because they do not play a role for the deformation we investigate.

Legendre polynomials are used in order to comply with the orthogonality condition defined in Reference 1, which requires

$$\int_V \mathbf{S}^T \tilde{\mathbf{E}} \, dV = 0, \tag{40}$$

where $\mathbf{S}$ denotes the second Piola-Kirchhoff stress tensor. For the enhancement $\tilde{\mathbf{E}}^2$, this simplifies to

$$\int_V S^{33} \tilde{E}_{33} \, dV = 0. \tag{41}$$

To ensure that S^{33} includes at least constant functions, the condition

$$\int_{-1}^{1} \left(\alpha_1 \zeta + \alpha_2 L_2(\zeta)\right) d\zeta = 0 \qquad \forall \alpha_1, \alpha_2, \tag{42}$$

has to be fulfilled. This condition is fulfilled since

$$\int_{-1}^{1} \zeta \, d\zeta = 0 \qquad \text{and} \qquad \int_{-1}^{1} L_2(\zeta) \, d\zeta = 0, \tag{43}$$

hold. With the enhancement from (38), the trace of the enhanced strain tensor $\mathbf{E}^2 = \mathbf{E}^{\mathrm{u}} + \tilde{\mathbf{E}}^2$ is

$$\text{tr } \mathbf{E}^2 = k_1 \zeta + \frac{1}{2} k_1^2 \zeta^2 + c + \alpha_1 \zeta + \alpha_2 L_2(\zeta), \tag{44}$$

and Equation (10b) becomes

$$c + \alpha_1 \zeta + \alpha_2 L_2(\zeta) \stackrel{!}{=} -k_1 \zeta - \frac{1}{2} k_1^2 \zeta^2. \tag{45}$$

The free parameters α_1, α_2, and c can take values such that (45) is fulfilled for every $\zeta \in [-1, 1]$, that is, the isochoric condition (10b) can be fulfilled at an arbitrary number of integration points N_{GP}^{ζ}. Thus, the standard element formulation needs two EAS parameters to be free from NPS in the trE case.

Th above findings on the behavior of the standard element formulation can be easily generalized to an arbitrary displacement field. In any case, $E_{11}(\zeta)$ and $E_{22}(\zeta)$ can be at most quadratic functions in ζ, which requires $E_{33}(\zeta)$ to be a quadratic function in ζ as well. This is achieved by the additional eighth EAS parameter, as shown above.

3.5 | Nonlinear Poisson stiffening effect—detF case

3.5.1 | Analysis of the effect

For the detF case from Table 1 we again investigate the behavior of the generic 3d-shell elements presented in Section 3.3, without the eighth parameter proposed in Section 3.4.2. We evaluate (10c) for the deformation given in (17). Using the results from $(34)_1$, this yields

$$c + \alpha_1 \zeta \stackrel{!}{=} -\frac{2k_1 \zeta + k_1^2 \zeta^2}{2 + 4k_1 \zeta + 2k_1^2 \zeta^2} =: h(\zeta), \tag{46}$$

for the standard element formulation and with $(34)_2$ we obtain

$$c + \alpha_1 \zeta \stackrel{!}{=} -\frac{2k_1 \zeta}{2 + 4k_1 \zeta} =: h_{\mathrm{red}}(\zeta), \tag{47}$$

for the reduced element formulation. The left-hand side of (46) and (47) is a linear function in ζ and the function on the right-hand side is a rational function with an infinite Taylor series. Therefore, they cannot be equal in the entire range $\zeta \in [-1, 1]$. To derive an upper bound for

$$|r_{\mathrm{detF}}| = |c + \alpha_1 \zeta + h(\zeta)|, \tag{48}$$

we use the Taylor expansion of h:

$$h(\zeta) = \sum_{p=1}^{\infty} \frac{p+1}{2} (-k_1)^p \zeta^p, \tag{49}$$

$$h_{\mathrm{red}}(\zeta) = \sum_{p=1}^{\infty} (-k_1)^p 2^{p-1} \zeta^p. \tag{50}$$

Inserting (49) and (50) into the residual from (48) yields

$$|r_{\text{detF}}| = \left| c + \alpha_1 \zeta + \sum_{p=1}^{\infty} \frac{p+1}{2}(-k_1)^p(\zeta)^p \right| \le |c| + \left|(\alpha_1 - k_1)\zeta\right| + \sum_{p=2}^{\infty} \left| \frac{p+1}{2}(-k_1)^p(\zeta)^p \right|, \tag{51}$$

$$|r_{\text{detF}}^{\text{red}}| = \left| c + \alpha_1 \zeta + \sum_{p=1}^{\infty}(-k_1)^p 2^{p-1}(\zeta)^p \right| \le |c| + \left|(\alpha_1 - k_1)\zeta\right| + \sum_{p=2}^{\infty} \left|(-k_1)^p 2^{p-1}(\zeta)^p \right|. \tag{52}$$

Choosing $c = 0$ and $\alpha_1 = k_1$ minimizes the upper bounds and yields

$$|r_{\text{detF}}^{\text{opt}}| \le \sum_{p=2}^{\infty} \left| \frac{p+1}{2} k_1^p (\zeta)^p \right| \in \mathcal{O}\left((k_1 \zeta)^2\right), \tag{53}$$

$$|r_{\text{detF}}^{\text{red,opt}}| \le \sum_{p=2}^{\infty} \left| k_1^p 2^{p-1}(\zeta)^p \right| \in \mathcal{O}\left((k_1 \zeta)^2\right). \tag{54}$$

From the results in (46)–(54), we can identify properties of NPS in the detF case, that is using a material model with $\mathcal{W}_{\text{vol}}$ depending on det $\mathbf{F}$. Similar to the trE case, (46) and (47) can be understood as a polynomial interpolation problem: find c, α_1 such that $c + \alpha_1 \zeta_i = h(\zeta)$ for all N_{GP}^{ζ} integration point locations ζ_i. This problem has a unique solution for $N_{\text{GP}}^{\zeta} = 2$, such that both the standard and the reduced formulation are free from NPS. For a larger number of integration points, there is no solution and thus *both* formulations, the standard and reduced one, suffer from NPS in the detF case. We expect the residual to be in the same order of magnitude as for the trE case.

In summary, the following observations can be made for the detF case:

- In contrast to the trE case, the reduced formulation is not always free from NPS in the detF case.
- Whether or not NPS occurs, depends on the number of Gauss points N_{GP}^{ζ} in ζ-direction.
- If $N_{\text{GP}}^{\zeta} = 2$, both element formulations are free from NPS.
- If $N_{\text{GP}}^{\zeta} \ge 3$, both element formulations suffer from NPS.

3.5.2 | Methods to avoid NPS in the detF case

In this section, we discuss how the influence of NPS on the solution can be weakened in the detF case. In the trE case, a possible solution strategy is to introduce one additional EAS parameter. In the detF case, the isochoric conditions (46) and (47) require E_{33} to be equal to a rational function. No matter how many EAS parameters we add, there always remains a difference between the polynomial E_{33} and the rational function $h(\zeta)$. Let now m be the number of EAS parameters used to enhance E_{33} and

$$\mathbf{E}^m = \mathbf{E}_u + \tilde{\mathbf{E}}^m, \qquad \mathbf{E}^{\text{red},m} = \mathbf{E}_u^{\text{red}} + \tilde{\mathbf{E}}^{\text{red},m}, \tag{55}$$

the enhanced strain tensors for the standard and reduced element formulation, respectively. The EAS contribution

$$\tilde{\mathbf{E}}^{\text{red},m} = \tilde{\mathbf{E}}^m = \mathbf{B}_e^m \boldsymbol{\alpha}^m, \tag{56}$$

can be written as a product of the enhanced strain displacement matrix $\mathbf{B}_e^m$ and the vector $\boldsymbol{\alpha}^m$, containing the DOFs related to the enhanced strain,

$$\mathbf{B}_e^m = \begin{bmatrix} 0 & 0 & \zeta & 0 & 0 & 0 \\ 0 & 0 & L_2(\zeta) & 0 & 0 & 0 \\ \vdots & \vdots & \vdots & \vdots & \vdots & \vdots \\ 0 & 0 & L_m(\zeta) & 0 & 0 & 0 \end{bmatrix}^T, \qquad \boldsymbol{\alpha}^m = \begin{bmatrix} \alpha_1 & \alpha_2 & \dots & \alpha_m \end{bmatrix}^T, \qquad L_m(\zeta): \text{Legendre polynomials}. \tag{57}$$

Again, Legendre polynomials $L_m(\zeta)$ are chosen for the enhancement in order to satisfy the orthogonality condition, as explained in Section 3.4.2. The isochoric condition (10c) can then be written as

$$c + \sum_{i=1}^{m} \alpha_i L_i(\zeta) \overset{!}{=} h(\zeta). \tag{58}$$

Similar to (46) and (47), Equation (58) can be understood as a polynomial interpolation problem. Due to the additional EAS parameters, the left-hand side is now a polynomial of order m. A unique solution for the free parameters c and α_i exists, that satisfies (58) at $m + 1$ locations in ζ-direction. Transferred to NPS in the detF case, this means that if we use m EAS parameters to enhance E_{33} and $N_{\text{GP}}^{\zeta} \leq m + 1$, the element does not suffer from NPS. If $N_{\text{GP}}^{\zeta} > m + 1$, the isochoric condition cannot be fulfilled at all integration points and NPS has to be expected.

Regarding the optimal case bound for the residual, adding EAS parameters is also beneficial:

$$|r_{\text{detF}}| = \left| c + \sum_{i=1}^{m} \alpha_i L_i + \sum_{p=1}^{\infty} \frac{p+1}{2}(-k_1)^p(\zeta)^p \right| \leq |c| + \underbrace{\left| \sum_{p=1}^{m} \left(\alpha_p L_p + \frac{p+1}{2}(-k_1)^p(\zeta)^p \right) \right|}_{(*)} + \sum_{p=m+1}^{\infty} \left| \frac{p+1}{2}(-k_1)^p(\zeta)^p \right|, \tag{59}$$

$$|r_{\text{detF}}^{\text{red}}| = \left| c + \sum_{i=1}^{m} \alpha_i L_i + \sum_{p=1}^{\infty} (-k_1)^p 2^{p-1}(\zeta)^p \right| \leq |c| + \underbrace{\left| \sum_{p=1}^{m} \left(\alpha_p L_p + (-k_1)^p 2^{p-1}(\zeta)^p \right) \right|}_{(*)} + \sum_{p=m+1}^{\infty} \left| (-k_1)^p 2^{p-1}(\zeta)^p \right|. \tag{60}$$

It is possible to choose c and α_p such that the contributions marked with (*) vanish and the error bounds for the optimal case become

$$|r_{\text{detF}}^{h,\text{opt}}| \leq \sum_{p=m+1}^{\infty} \left| k_1^p 2^{p-1}(\zeta)^p \right| \in \mathcal{O}\left((k_1 \zeta)^{m+1}\right), \tag{61}$$

$$|r_{\text{detF}}^{h_{\text{red}},\text{opt}}| \leq \sum_{p=m+1}^{\infty} \left| \frac{p+1}{2} k_1^p(\zeta)^p \right| \in \mathcal{O}\left((k_1 \zeta)^{m+1}\right). \tag{62}$$

This dependency of the optimal case error bound on the number of EAS parameters m indicates that the influence of the stiffening effect decreases with an increasing number of EAS parameters because $|k_1| \leq 1$ and $|\zeta| \leq 1$.

In the detF case, we are unable to completely eliminate the NPS effect for an *arbitrary* number of integration points by adding a given *finite* number of EAS parameters. Depending on the specific problem, we might need a certain number of EAS parameters to reduce the error to an acceptable level. Therefore, alternative approaches that fully avoid NPS in the detF case would be attractive. Possible solutions could be to use a different functional, for example, to use a displacement-pressure element[21] or an element based on a Hellinger–Reissner functional.[22] Whether such approaches are capable of fully avoid NPS is subject to current investigations.

3.6 | Extension to other element types and other nonlinear strain measures

Although this article focuses on 3d-shell elements, the theory of the NPS effect can be transferred to other element types, for example, two-dimensional plain strain elements with 3×3 integration points. The authors are currently investigating the influence of the stiffening effect for such element types.

The analysis shown in the previous sections can also be extended to other geometrically nonlinear strain measures. Within our research, we investigated a 3d-shell element that is available in the commercial software LS-DYNA as shell element no. 25. It is an extension of the 5-parameter shell element presented in Reference 23. Shell element no. 25 is formulated based on velocity strains (rate of deformation). We assume a velocity field with the same properties as the bending-like displacement field (17):

$$v_2 = 0 \qquad \text{no deformation in } \eta - \text{direction}, \tag{63a}$$

$$v_3 = v_3(\zeta) \qquad v_3 \text{ is independent of } \xi \text{ and } \eta. \tag{63b}$$

In this section we limit ourselves to the case where the isochoric condition is represented by the trace of the velocity strain tensor:

$$\mathrm{tr}\,\mathbf{d} = d_{11} + d_{22} + d_{33} = \frac{\partial v_1}{\partial x_1} + \frac{\partial v_2}{\partial x_2} + \frac{\partial v_3}{\partial x_3}. \tag{64}$$

According to Reference 24, the geometry of the current configuration for this element is given by

$$\mathbf{x} = (\mathbf{x}_I + s_I \mathbf{n})\, N_I\,(\xi, \eta), \tag{65}$$

and the velocity field is described by

$$\mathbf{v} = (\mathbf{v}_I + s_I \boldsymbol{\omega}_I \times \mathbf{n} + \dot{s}_I \mathbf{n})\, N_I\,(\xi, \eta), \tag{66}$$

where I indicates the node number and the sum is taken over I. The values t_I represent the thickness at node I and q_I allows for linear transverse normal strain. These are combined to

$$s_I = \frac{\zeta}{2} t_I + \left(1 - \zeta^2\right) q_I, \tag{67}$$

which describes the linear and quadratic part of the displacement field in thickness direction at node I. Bilinear Lagrangian shape functions $N_I\,(\xi, \eta)$ are used to interpolate between the nodal values. Furthermore, $\mathbf{n} = \begin{bmatrix} 0 & 0 & 1 \end{bmatrix}^{\mathrm{T}}$ is the shell normal in the local coordinate system. Using these quantities, the velocity gradient for this element in a local coordinate system is, according to Reference 24, given by

$$\frac{\partial \mathbf{v}}{\partial \mathbf{x}} = (\mathbf{v}_I + s_I \boldsymbol{\omega}_I \times \mathbf{n} + \dot{s}_I \mathbf{n})\, \frac{\partial N_I}{\partial \mathbf{x}} + \left(\boldsymbol{\omega}_I \times \mathbf{n}\, \frac{\partial s_I}{\partial \mathbf{x}} + \mathbf{n}\, \frac{\partial \dot{s}_I}{\partial \mathbf{x}} \right) N_I. \tag{68}$$

For the case of the director being normal to the midsurface of the element, the third component of $\frac{\partial N_I}{\partial \mathbf{x}}$ is zero, $\frac{\partial N_I}{\partial x_3} = 0$. In Reference 24 it is assumed that this term is also approximately zero in the general case and it is therefore neglected in the implementation of the element. With

$$\boldsymbol{\omega}_I \times \mathbf{n} = \begin{bmatrix} \omega_{1I} \\ \omega_{2I} \\ \omega_{3I} \end{bmatrix} \times \begin{bmatrix} 0 \\ 0 \\ 1 \end{bmatrix} = \begin{bmatrix} \omega_{2I} \\ -\omega_{1I} \\ 0 \end{bmatrix}, \tag{69}$$

we find

$$\frac{\partial v_1}{\partial x_1} = (v_{1I} + s_I \omega_{2I})\, \frac{\partial N_I}{\partial x_1} + \omega_{2I}\, \frac{\partial s_I}{\partial x_1} N_I, \tag{70a}$$

$$\frac{\partial v_2}{\partial x_2} = 0, \tag{70b}$$

$$\frac{\partial v_3}{\partial x_3} = \frac{\partial \dot{s}_I}{\partial x_3} N_I. \tag{70c}$$

Equation (63b) defines the thickness velocity

$$v_3 = (v_{3I} + \dot{s}_I\,(\zeta))\, N_I\,(\xi, \eta), \tag{71}$$

to be independent of ξ and η. Therefore, all v_{3I} need to take on the same value $\bar{v}_3$. The same holds for t_I and q_I from Equation (67). Then, the time derivative of s_I from Equation (67) becomes

$$\dot{s}_I = \dot{s} = \frac{\zeta}{2} \dot{t} + \left(1 - \zeta^2\right) \dot{q}, \tag{72}$$

and s_I itself can be written as

$$s_I = \bar{s} = \frac{\zeta}{2}\bar{t} + \left(1 - \zeta^2\right)\bar{q}. \tag{73}$$

The geometry description in the deformed configuration from (65) then becomes

$$\mathbf{x} = \mathbf{x}_I N_I (\xi, \eta) + \bar{s}\mathbf{n}. \tag{74}$$

The resulting Jacobian is

$$\mathbf{J} = \frac{\partial \mathbf{x}}{\partial \boldsymbol{\xi}} = \begin{bmatrix} x_{1I}\frac{\partial N_I}{\partial \xi} & x_{2I}\frac{\partial N_I}{\partial \xi} & 0 \\ x_{1I}\frac{\partial N_I}{\partial \eta} & x_{2I}\frac{\partial N_I}{\partial \eta} & 0 \\ 0 & 0 & \frac{t}{2} - 2q\zeta \end{bmatrix}, \tag{75}$$

with its inverse

$$\mathbf{J}^{-1} = \begin{bmatrix} J_{11}^{-1} & J_{12}^{-1} & 0 \\ J_{21}^{-1} & J_{22}^{-1} & 0 \\ 0 & 0 & \frac{2}{t-4q\zeta} \end{bmatrix}, \tag{76}$$

which allows us to simplify the derivative $\frac{\partial s_I}{\partial x_1}$ required in (70a):

$$\frac{\partial s_I}{\partial x_1} = \frac{\partial \bar{s}}{\partial x_1} = \underbrace{\frac{\partial \bar{s}}{\partial \xi}\frac{\partial \xi}{\partial x_1}}_{=0} + \underbrace{\frac{\partial \bar{s}}{\partial \eta}\frac{\partial \eta}{\partial x_1}}_{=0} + \underbrace{\frac{\partial \bar{s}}{\partial \zeta}\frac{\partial \zeta}{\partial x_1}}_{=0} = 0. \tag{77}$$

With the results from (72), (73), (76), and (77), Equations (70a) and (70c) can be simplified to

$$d_{11} = \frac{\partial v_1}{\partial x_1} = (v_{1I} + s\omega_{2I})\frac{\partial N_I}{\partial x_1} \in \mathcal{O}\left((\zeta)^2\right), \tag{78}$$

$$d_{33} = \frac{\partial v_3}{\partial x_3} = \frac{\partial \dot{s}}{\partial \zeta}\frac{\partial \zeta}{\partial x_3} = \frac{\dot{t} - 4\dot{q}\zeta}{t - 4q\zeta}. \tag{79}$$

We find that d_{11} is a quadratic function in ζ because $\frac{\partial N_I}{\partial x_1}$ is independent of ζ and s is a quadratic function in ζ. In contrast to this, d_{33} is a rational function. Since

$$\text{tr } \mathbf{d} = d_{11} + d_{33} \neq 0, \tag{80}$$

this element suffers from NPS, if a strain energy function based on tr $\mathbf{d}$ is used along with higher order through-the-thickness integration ($N_{\text{GP}}^{\zeta} \geq 3$). The overly stiff behavior of this element has been discovered in Reference 13, but it could not be explained by that time. For the element discussed in this section, NPS can be avoided by modifying the kinematic description and the strain such that the element is able to satisfy the isochoric condition of the underlying material model, as it has been extensively discussed for the Green–Lagrange strain in Section 3.4.2. A detailed investigation of such a modification can be found in Reference 25.

3.7 | Summary of theoretical observations

The theoretical derivations regarding the NPS effect can be summarized as follows. Depending on the strain energy function $\mathcal{W}$ of the material model, three different cases have to be distinguished:

1. $\mathcal{W}_{\text{vol}}$ depends on tr ε (trε case): An element based on a 6-parameter shell model suffers from LPS, whereas an element based on a 7-parameter shell model, which includes linear transverse normal strain in thickness direction, is free from LPS. This is already well known since the 1990s.

2. $\mathcal{W}_{\text{vol}}$ depends on tr $\mathbf{E}$ (trE case): An element based on a 7-parameter shell model is free from NPS only if the parts of the strain tensor that are quadratic w.r.t. the thickness coordinate are neglected or if $N_{\text{GP}}^{\zeta} < 3$. In case the quadratic strain component is included and $N_{\text{GP}}^{\zeta} \geq 3$, a 7-parameter shell element suffers from NPS. The impact of the NPS effect on the solution is smaller than the impact of LPS. This can be seen from a comparison of the residuals of the isochoric conditions in (21) and (37). While the residual in the trε case depends on the magnitude of the displacement k_1, it depends on k_1^2 in the trE case, which makes the stiffening effect less severe for $|k_1| \ll 1$. An element based on an 8-parameter shell model that includes linear and quadratic transverse normal strain is free from LPS and NPS.

3. $\mathcal{W}_{\text{vol}}$ depends on det $\mathbf{F}$ (detF case): NPS can only be prevented by using a combination of m EAS parameters together with $N_{\text{GP}}^{\zeta} = m + 1$. For $N_{\text{GP}}^{\zeta} > m + 1$, the element suffers from NPS. In this case, the NPS effect decreases with increasing m. Choosing $N_{\text{GP}}^{\zeta} < m + 1$ is not an option because $N_{\text{GP}}^{\zeta} \geq m + 1$ is required for a full integration of the stiffness matrix. Alternative options to prevent NPS in the detF case are mentioned at the end of Section 3.5.

4 | NUMERICAL EXAMPLES

4.1 | Virtual ring test

4.1.1 | Problem setup

To provide numerical evidence of the theoretical derivations from Section 3, we use a virtual ring test, similar to the test performed in Reference 13, as a test example. We omit to investigate the (geometrically linear) trε case numerically, as this case is already well known. Figure 3 shows the setup of the virtual ring test. A slit cylindrical tube with infinite length in Y-direction is investigated. For the simulation, a representative strip of width 1 of the tube is taken and plain strain boundary conditions are applied in Y-direction. The virtual ring is clamped at A and is split at B. Both ends of the ring are drawn in opposite direction using inhomogeneous Dirichlet boundary conditions. The radius, measured at A, continuously decreases and imposes a bending-dominated deformation in the vicinity of A. The dimensions are $t = 1$, $r_0 = 5$ and $u(t)$ increases linearly from $\hat{u} = 0$ to $\hat{u} = 10$ and is applied in X-direction. Figure 4 shows the deformed configuration for $\hat{u} = 10$. For all numerical examples, we use implementations of material models provided by the material library MUESLI.[26] Young's modulus is $E = 1000$, Poisson's ratio ν and N_{GP}^{ζ} vary. The structure is discretized with 60 solid shell elements in circumferential direction and one element in both thickness direction and Y-direction, as shown in Figure 4.

A nonlinear static analysis is performed. The main quantity of interest is the reaction force in X-direction at either end of the slit ring

$$F = \sum_{i=1}^{4} F_i, \tag{81}$$
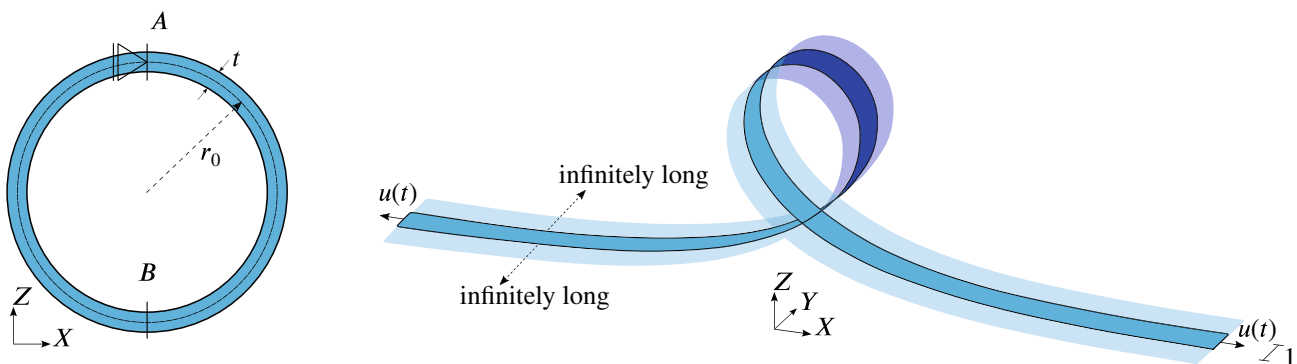
FIGURE 3 Virtual ring test: Projection of the initial geometry onto the X-Z-plane (left); sketch of the midsurface of the deformed configuration with prescribed displacement boundary conditions $u(t)$ (right): a strip of an infinitely long slit cylindrical tube is simulated (opaque geometry on the right).
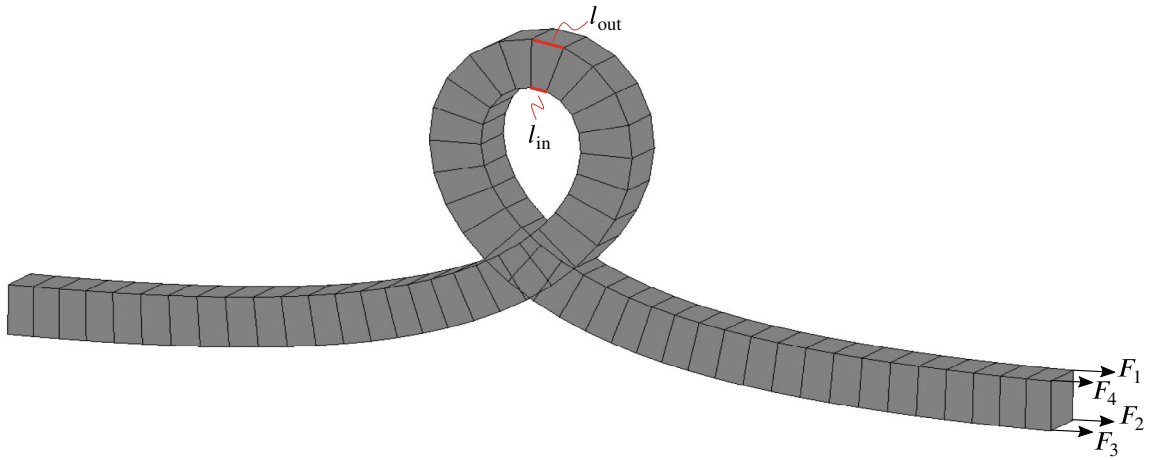
FIGURE 4 Virtual ring test: Deformed configuration for a displacement of $\hat{u} = 10$ discretized with 60 elements in circumferential direction.

with forces F_i shown in Figure 4. We investigate several element formulations, which are implemented in the authors' in-house finite element research code. We follow the naming conventions in the original publications and add a suffix "EAS-m" that indicates that the enhanced strain displacement matrix $\mathbf{B}_e$ of an element contains the enhancements $\mathbf{B}_e^m$ defined in (57). The investigated element formulations are:

- **Shell10-EAS-m**: Shell10 is a solid-shell element with quadratic strain in ζ-direction, proposed in Reference 14. It uses $N_{\mathrm{GP}}^\xi = N_{\mathrm{GP}}^\eta = 2$ and arbitrary N_{GP}^ζ for numerical integration. To prevent transverse shear locking and trapezoidal locking, the ANS method is used and Shell10 uses EAS to prevent in-plane shear locking and in-plane volumetric locking. Its original formulation has three EAS parameters to prevent Poisson stiffening. These are related to the enhanced strains ζ, $\xi\zeta$ and $\eta\zeta$. Therefore, $\mathbf{B}_e$ of this element contains $\mathbf{B}_e^1$ and we refer to this formulations as Shell10-EAS-1.

- **Q1STs-EAS-m**: Q1STs is a solid-shell element proposed in Reference 15. It was developed with the goal of efficiently performing forming simulations with elasto-plastic material behavior. Recently, extensions of this element formulation towards gradient-extended damage have been presented in References 27 and 28. It uses reduced integration with one integration point in the shell plane and an arbitrary number of integration points in thickness direction. The element is developed based on a Taylor series of the strain tensor. Its strain tensor can be written as

$$\mathbf{E} = \mathbf{E}^0 + \zeta\mathbf{E}^\zeta + \zeta^2\mathbf{E}^{\zeta\zeta} + \xi\mathbf{E}^\xi + \eta\mathbf{E}^\eta + \xi\eta\mathbf{E}^{\xi\eta} + \eta\zeta\mathbf{E}^{\eta\zeta} + \xi\zeta\mathbf{E}^{\xi\zeta}. \tag{82}$$

The ANS method is used to prevent transverse shear locking and trapezoidal locking. The original formulation's enhanced strain displacement matrix $\mathbf{B}_e$ is identical to $\mathbf{B}_e^1$ and the original element is therefore referred to as Q1STs-EAS-1.

- **Q1STs-red-EAS-m**: Q1STs-part is a modified version of Q1STs in which the quadratic part of the strain $\zeta^2\mathbf{E}^{\zeta\zeta}$ is neglected, that is, its strain tensor can be written as

$$\mathbf{E} = \mathbf{E}^0 + \zeta\mathbf{E}^\zeta + \xi\mathbf{E}^\xi + \eta\mathbf{E}^\eta + \xi\eta\mathbf{E}^{\xi\eta} + \eta\zeta\mathbf{E}^{\eta\zeta} + \xi\zeta\mathbf{E}^{\xi\zeta}. \tag{83}$$

Apart from this, the element is identical to Q1STs-EAS-m. This version of the element has been investigated in one numerical example in Reference 15.

The original publications for these elements only provide element formulations EAS-1 according to the definition above. Versions with $m \geq 2$ are neither suggested nor investigated. We chose the Q1STs elements among many elements available in the literature, because the quadratic strain in thickness direction that might cause NPS can be easily excluded.

Our aim is solely to investigate NPS by using various material models, Poisson's ratios and varying N_{GP}^ζ. A general investigation of the elements' performance for various problems can be found in the original publications and will not be repeated within this article.

TABLE 2 Virtual ring test: Reaction force F for $u = \hat{u}$ with a SVK material model.

Element	N_{GP}^{ζ}	$\nu = 0$	$\nu = 0.4$	$\nu = 0.49$	$\nu = 0.499$	$\nu = 0.4995$	NPS
Shell10-EAS-1	2	8.738	10.746	12.041	12.203	12.212	No
Shell10-EAS-1	3	8.697	10.743	12.696	17.721	21.680	Yes
Shell10-EAS-2	3	8.697	10.696	11.986	12.148	12.157	No

Note: Various versions of Shell10-EAS-m with varying m and varying N_{GP}^{ζ} are investigated. The column "NPS" indicates whether this variant suffers from NPS or not.
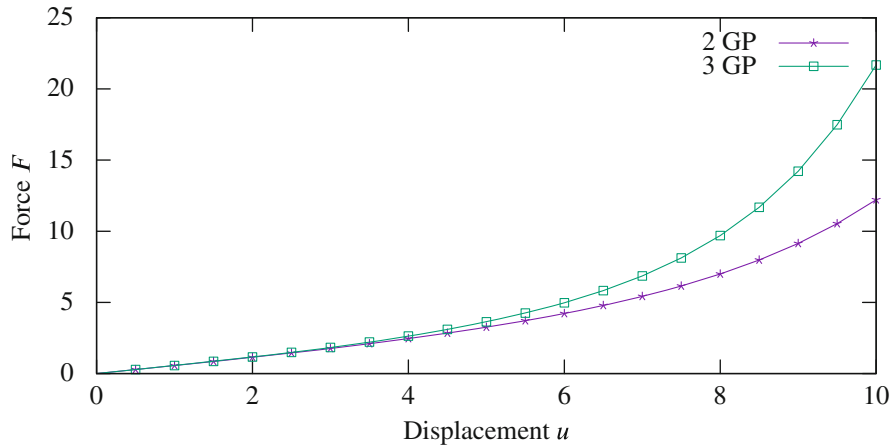
FIGURE 5 Virtual ring test: Force displacement curve for Shell10 with $N_{GP}^{\zeta} = 2$ and $N_{GP}^{\zeta} = 3$. The SVK material model with Poisson's ratio $\nu = 0.4995$ is used.

4.1.2 | St. Venant-Kirchhoff material model—trE case

To confirm our theoretical derivations for the trE case, explained in Section 3.4, we use a St. Venant-Kirchhoff (SVK) material model. Table 2 shows the reaction force F for various versions of Shell10. For $\nu = 0$ and $\nu = 0.4$, the results for all variants are similar. For $\nu \geq 0.499$ the variant with $m = 1$ and three GP, which suffers from NPS, shows a significantly higher reaction force compared to the other variants.

The force displacement curve for $\nu = 0.4995$ in Figure 5 shows almost no difference between the solutions with $N_{GP}^{\zeta} = 2$ and $N_{GP}^{\zeta} = 3$ for small displacements and resulting small strains up to approximately $u = 4$. For larger displacements and resulting larger strain a significant deviation between both solutions becomes visible. As explained in the Section 3.4, a 3d-shell element which includes quadratic strain in ζ suffers from NPS, if more than two integration points in thickness direction are used. This is the case for Shell10-EAS-1 with three integration points through the thickness. The modified version Shell10-EAS-2 with an additional EAS parameter that allows for a quadratic transverse normal strain field ($m = 2$) does not suffer from NPS. Its results are close to results for $m = 1$ and $N_{GP}^{\zeta} = 2$. The fact that even for an almost incompressible material behavior ($\nu = 0.4995$) no difference is visible for small strains ($u < 4$) confirms that NPS is less severe than its linear counterpart. Nevertheless, the significant difference for large strains ($u = 10$) emphasizes the importance of this stiffening effect for the case of large bending deformations.

Table 3 shows the results for the same setup with various version of Q1STs-EAS-m. All variants show similar results, except the standard variant with $m = 1$ and $N_{GP}^{\zeta} = 3$. Due to NPS, it shows a significantly higher reaction force for $\nu \geq 0.499$. The other variants including quadratic strain are free from NPS, because they use only two integration points in thickness direction or an additional EAS parameter prevents NPS, respectively. As explained in the theoretical derivations, the quadratic part in ζ of the transverse normal strain causes NPS. Consequently, the reduced variant of the element, which neglects quadratic strain in ζ, does not suffer from NPS in the trE case. This element formulation provides exactly the same results for $N_{GP}^{\zeta} = 2$ and $N_{GP}^{\zeta} = 3$. Due to the Taylor series, this element is based on, the internal forces can be integrated exactly with two integration points. Therefore, the results for two and tree (and more) integration points are identical in this test.

TABLE 3 Virtual ring test: Reaction force for various versions of Q1STs-EAS-m for $u = \hat{u}$ with SVK material model.

Element	N_{GP}^{ζ}	$v = 0$	$v = 0.4$	$v = 0.49$	$v = 0.499$	$v = 0.4995$	NPS
Q1STs-EAS-1	2	9.063	11.128	12.464	12.632	12.641	No
Q1STs-EAS-1	3	9.078	11.158	12.690	14.799	16.883	Yes
Q1STs-EAS-2	3	9.078	11.145	12.482	12.649	12.659	No
Q1STs-red-EAS-1	2 or 3	9.067	11.106	12.427	12.593	12.602	No

TABLE 4 Virtual ring test: Reaction force for various versions of Q1STs-red-EAS-m for $u = \hat{u}$ with a Neo-Hookean material model.

N_{GP}^{ζ}	$m = 1$	$m = 2$	$m = 3$	$m = 4$	$m = 5$
2	11.401	-	-	-	-
3	32.692	12.161	-	-	-
4	32.936	14.875	12.229	-	-
5	32.942	14.911	12.514	12.236	-
6	32.942	14.913	12.521	12.260	12.260
7	32.942	14.913	12.522	12.261	12.261

Note: Note that a full integration of $\int_{\Omega} \left(\mathbf{B}_e^m\right)^T \mathbf{C} \left(\mathbf{B}_e^m\right) d\Omega$ with $\mathbf{C}$ being constant w.r.t. ζ requires $N_{GP}^{\zeta} = m + 1$ and therefore the upper diagonal part of the table is empty.

4.1.3 | Neo-Hooke material model—detF case

To investigate the element behavior in the detF case, we carry out the virtual ring test with a Neo-Hookean material model and the element formulation Q1STs-red. This element does not suffer from NPS in the trE case and its results are even independent of N_{GP}^{ζ}. In contrast to the standard Q1STs element, this allows us to isolate the stiffening caused by the use of the Neo-Hookean material model from the stiffening caused by the quadratic strain.

As we are investigating Poisson stiffening effects, the impact depends on Poisson's ratio. This has been validated by numerical examples for the SVK material model (see Tables 2 and 3). Instead of repeating this analysis for a Neo-Hookean material model, our focus in the analysis of the detF case is on the influence of the number of EAS parameters and the number of integration points N_{GP}^{ζ}. Table 4 shows the result of the virtual ring test for various combinations of m and N_{GP}^{ζ} for $v = 0.499$. A significantly stiffer behavior with $N_{GP}^{\zeta} = m + 2$ compared to $N_{GP}^{\zeta} = m + 1$ is clearly visible in the numerical results. This shows that Q1STs-red suffers from NPS, if a Neo-Hookean material model is used together with $N_{GP}^{\zeta} \geq m + 2$, as it was theoretically predicted in Section 3.5.

Moreover, Table 4 shows that the difference between the solution with $N_{GP}^{\zeta} = m + 1$ and $N_{GP}^{\zeta} = m + 2$ decreases for increasing m, that is, the error caused by NPS decreases. In this example, it is practically negligible for $m \geq 4$. In Section 3.5, it has been shown that the optimal error bound decreases with an increasing number of EAS parameters. This leads to the expectation that the influence of the stiffening effect decreases when the number of EAS parameters increases. This idea is supported by the numerical results in Table 4. Nevertheless, it is important to understand that the magnitude of the difference between the solutions with $N_{GP}^{\zeta} = m + 1$ and $N_{GP}^{\zeta} = m + 2$ depends on the magnitude of the strain and the Poisson's ratio of the specific example. An analysis of the detF case using the standard Q1STs element shows qualitatively similar results.

4.1.4 | Analysis of influencing factors

The leading term of the upper bound for the residuals in the trE case (Equation 37) and in the detF case (Equations 53 and 54) is $k_1^2 \zeta^2$. Furthermore, the volumetric part of the strain energy function scales linearly with the bulk modulus (Equations 1a–1c). This indicates that there are three major factors influencing how severe the effect of NPS is: the bulk modulus, the magnitude of the deformation and thus the strain (represented by k_1 in the equations), and the location at

TABLE 5 Virtual ring test: Reaction force for various versions of Q1STs for $u = \hat{u}$ with SVK material model using three Lobatto points for numerical integration.

Element	$v = 0$	$v = 0.4$	$v = 0.49$	$v = 0.499$	$v = 0.4995$	NPS
Q1STs-EAS-1	9.102	11.202	13.028	17.883	22.559	Yes
Q1STs-EAS-2	9.102	11.169	12.508	12.676	12.685	No
Q1STs-red-EAS-1	9.067	11.106	12.427	12.593	12.602	No

which the residual is evaluated, namely the integration point locations, defined by the integration rule used (represented by ζ in the equations). The influence of these factors is investigated in the following numerical examples.

Integration rule

In the theoretical analysis of NPS, for example, in Section 3.4.1 for the trE case, we discussed the influence of the number of integration points, independently of the integration rule used. We used Gauss integration in all numerical examples presented so far. In order to investigate the influence of the integration rule, we investigate the reaction force using three Lobatto integration points. These integration points are located at $\zeta = 0$ with weight $\frac{4}{3}$ and at $\zeta = \pm 1$ with weight $\frac{1}{3}$ each. The results are shown in Table 5. The corresponding results with Gauss integration are shown in Table 3.

Q1STs-red-EAS-1 yields exactly the same result as for two or three Gauss integrations points. Both, integration with two Gauss points and integration with three Lobatto points, integrates polynomials up to third order exactly. As explained at the end of Section 4.1.2, using SVK material model, this element formulation can be integrated exactly with two Gauss integration points. It follows immediately that three Lobatto points yield the same result, free from NPS. The numbers for Q1STs-EAS-2 change slightly due to the change from Gauss to Lobatto integration rule, but this does not change the fact that Q1STs-EAS-2 is free from NPS in the trE case.

For Q1STs-EAS-1, NPS is even more pronounced when using Lobatto integration. For $v = 0.499$ and $v = 0.4995$, the element yields a significantly higher reaction force compared to the result using Gauss integration.

This is explained by the location of the outer Lobatto points. They are located at $\zeta = \pm 1$ whereas the outer points are located at $\zeta = \pm\sqrt{\frac{3}{5}}$ for a three point Gauss integration. The evaluation of the strains at integration points with larger absolute value of ζ in the Lobatto integration leads to a larger residual compared to Gauss integration, increasing the influence of NPS on the solution.

It can be concluded that the appearance of NPS only depends on the number of integration points used, but not on their positions and weights. Nevertheless, the position of the integration points affects how severe the influence of NPS is.

Bulk modulus

The results presented so far show that NPS depends strongly on Poisson's ratio and thus the bulk modulus. Figure 6 shows the relative error in the reaction force for $u = \hat{u}$ against an increasing bulk modulus for the element formulations Shell10-EAS-1 and Q1STs-EAS-1, both integrated with three Gauss points, and Q1STs-EAS-1 integrated with three Lobatto points. The relative error is calculated as

$$e = \frac{|F - F_{\text{ref}}|}{F_{\text{ref}}}, \tag{84}$$

where F_{ref} is the solution of the corresponding EAS-2 formulation. Since the absolute values of the bulk modulus are meaningless in this example, they are normalized such that $v = 0.4$ yields a normalized bulk modulus $K_{\text{norm}} = 1$. The data for these calculations can be found in Tables 2, 3, and 5.

Although the absolute value of the error differs depending on the element formulation and the integration rule used, the error scales approximately linearly with the bulk modulus. For comparison, a dashed line representing a linear increase of the error is shown in Figure 6.

Magnitude of deformation and strains

During the theoretical derivations, we introduced a parameter k_1 in Equation (17a) to describe the magnitude of the bending deformation. In order to investigate the magnitude of the bending deformation in the virtual ring test, we measure the length l_{out} of the outer edge and the length l_{in} of the inner edge in circumferential direction of the element at A, see
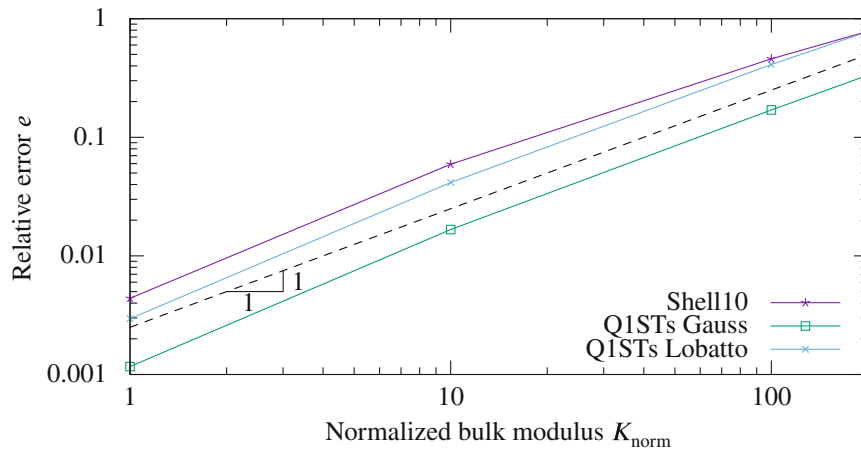
FIGURE 6   Virtual ring test: Relative error in the reaction force for various element formulations, evaluated for $u = \hat{u}$.

Figure 4. Let $l^0_{\text{in | out}}$ be $l_{\text{in | out}}$ evaluated for the undeformed configuration, then

$$l^0_{\text{M}} = \frac{1}{2} \left(l^0_{\text{out}} + l^0_{\text{in}} \right), \tag{85}$$

is the length of the corresponding edge of the midsurface. We measure the magnitude of the displacement related to bending as

$$\Delta l_{\text{B}} = \frac{1}{2} \left(\Delta l_{\text{out}} - \Delta l_{\text{in}} \right), \tag{86}$$

and construct a strain measure

$$E_{\text{B}} = \frac{\Delta l_{\text{B}}}{l^0_{\text{M}}} + \frac{1}{2} \left(\frac{\Delta l_{\text{B}}}{l^0_{\text{M}}} \right)^2, \tag{87}$$

which is similar to a 1d Green–Lagrange strain. This is of course not the real Green–Lagrange strain in the finite element, but rather a Green–Lagrange strain-like measure to quantify the amount of bending deformation. We choose to make the measurement in this particular element because it is the element with the highest bending strain in the deformed configuration.

Figure 7 shows the relative error in the reaction force as defined in Equation (84) plotted against the strain measure E_{B}. The error is calculated for Shell10-EAS-1 with three Gauss points and the solution of Shell10-EAS-1 with two Gauss points, which is free from NPS, serves as reference solution. Thickness t is varied as indicated in the legend of Figure 7 and maximum deformation $\hat{u} = 10$ and Poisson's ratio $\nu = 0.499$ are used unless otherwise stated in the legend.

The curves in the upper diagram of Figure 7 resemble each other very much. All three curves show approximately the same relative error for a given strain level. It follows that the relative error does not depend on the shell thickness. Nevertheless, NPS is more pronounced for thick shells, since a higher strain E_{B} occurs due to the larger shell thickness for a given final configuration. In the lower diagram of Figure 7, the relative error of two additional setups is compared to the relative error for $\nu = 0.499$ and $t = 1$. For a shell thickness of $t = 0.5$, higher strain levels are obtained by increasing the maximum displacement to $\hat{u} = 12$. Furthermore, a result with $t = 1$ but a smaller Poisson's ratio of $\nu = 0.49$ is shown in Figure 7. The bulk modulus for $\nu = 0.499$ is ten times higher than for $\nu = 0.49$ and the relative error scales approximately linearly with the bulk modulus, as shown in the previous section. Therefore, the error for the simulation with $\nu = 0.49$ shown in Figure 7 is significantly smaller than the error of the simulations with $\nu = 0.499$, but the shape of the curve is similar. A multiplication of the error for $\nu = 0.49$ by a factor of 10 in order to account for the bulk modulus difference, for example, evaluated at $E_{\text{B}} = 0.187$, yields $e = 0.267$, which is close to the error for $\nu = 0.499$ ($e = 0.254$).

Overall, a clear dependency of the relative error on the magnitude of the bending strain is visible in Figure 7 and this dependency is found to be similar for different variations of the virtual ring test. Figure 7 shows that a bending strain
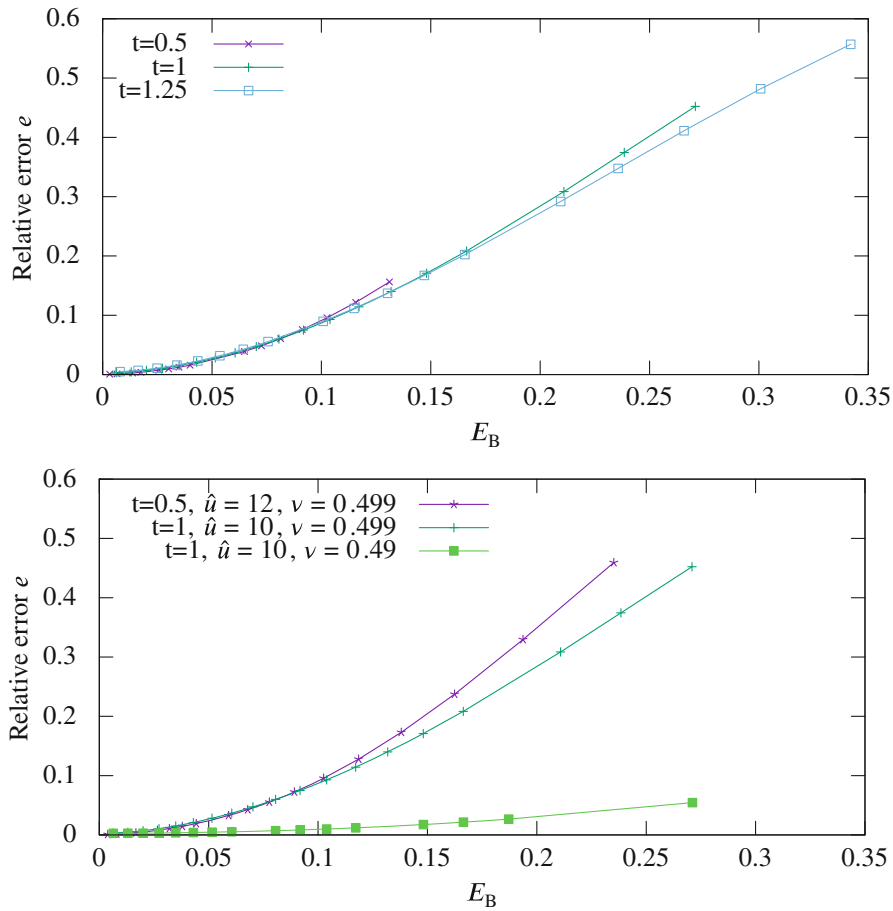
FIGURE 7 Virtual ring test: Relative error in the reaction force during the deformation process, plotted against the strain E_B.

$E_B \approx 0.1$ in combination a $v = 0.499$ is required to see a 10% error in the reaction force for the virtual ring test due to NPS. These numbers are of course specific for the virtual ring test, but they provide a general idea about the required parameter range in terms of Poisson's ratio and strain magnitude to make NPS visible in a benchmark. The requirements to make NPS clearly visible in a benchmark can be summarized as follows: a comparison of two integration points with more than two integration points needs to be performed or alternatively, EAS can be used to avoid NPS. Poisson's ratio must be chosen close to 0.5 and significant bending strain is required that dominates the system's response.

4.2 | Thick hyperelastic tube

Many of the numerical benchmarks available in the literature do not fulfill at least one of the aforementioned criteria. A benchmark already established in the literature, which satisfies many of these criteria, is the thick hyperelastic tube test.[29] NPS can be made visible in this test by varying Poisson's ratio. The problem setup and dimensions are given in Figure 8. The load is increased such that point M moves 16 cm in negative Z-direction. One quarter of the tube is simulated with a mesh of 6×16 elements. The Neo-Hookean material model implementation provided by the material library MUESLI[26] is used. It is based on the strain energy density function

$$\mathcal{W}(\mathbf{C}) = \frac{\lambda}{2}\left(\log\left(\sqrt{\det \mathbf{C}}\right)\right)^2 - \mu \log\left(\sqrt{\det \mathbf{C}}\right) + \frac{\mu}{2}(\mathrm{tr}\,\mathbf{C} - 3), \tag{88}$$

which is another notation for Equation (1c) and which is the same as in Reference 29. It differs slightly from the one used in Reference 15, see Equation (4). Originally, the test is conducted with $v = 0.4$. We vary this value between $v = 0$ and $v = 0.495$.
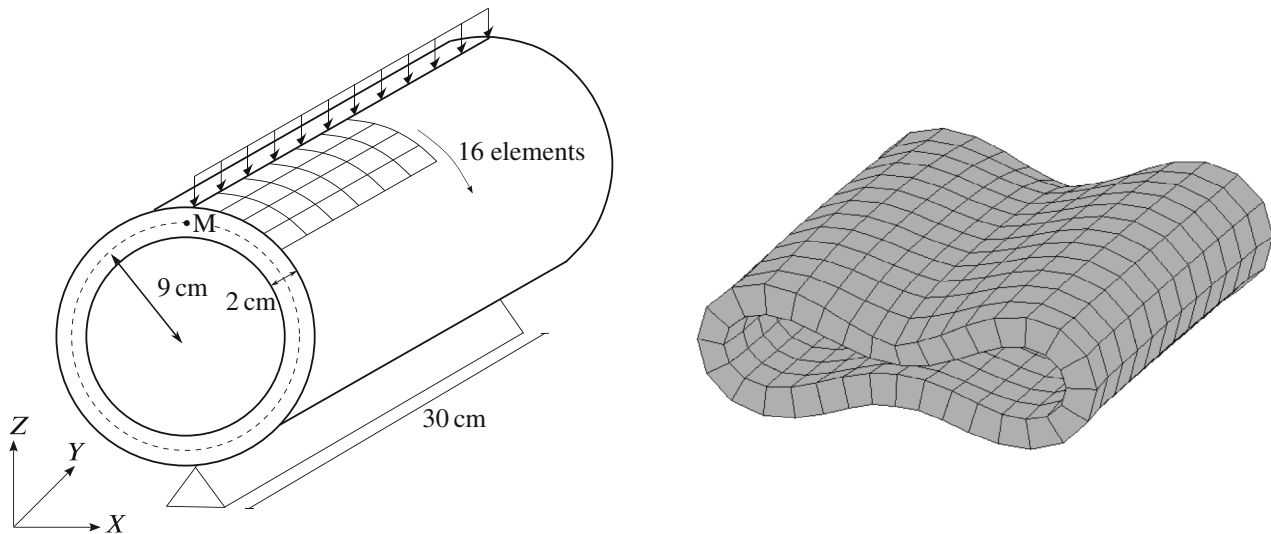
FIGURE 8 Hyperelastic tube test: Sketch of the test setup (left) and deformed geometry (right).

TABLE 6 Hyperelastic tube test: Reaction force for Q1STs-EAS-1 for two and three Gauss points.

Element	N_{GP}^{ζ}	$\nu = 0$	$\nu = 0.4$	$\nu = 0.49$	$\nu = 0.495$	NPS
Q1STs-EAS-1	2	27,221	28,552	29,805	29,890	No
Q1STs-EAS-1	3	27,375	29,222	36,746	41,869	Yes

Table 6 shows the results for the hyperelastic tube test. Similar to the results of the virtual ring test, the difference between the results for two and three integration points increases with the bulk modulus. For $\nu = 0$, this difference is due to the integration being more precise with three integration points. For $\nu = 0.4$, both the integration error and NPS play a role. As Poisson's ratio gets closer to 0.5, the difference becomes larger, which is clearly visible in the results for $\nu = 0.49$ and $\nu = 0.495$. In these cases, NPS significantly influences the results.

For the sake of completeness, it should be mentioned that the result reported in this article for $\nu = 0.4$ with three integration points differs minimally from the one reported in Reference 15 for the same configuration (29,222 compared to 29,179, 0.14% difference) due to the different strain energy density functions used. Furthermore, Reference 15 shows a stiffer behavior of Q1STs-red-EAS-1 compared to Q1STs-EAS-1 in the hyperelastic tube example. Our findings do not contradict this result. Even if there was a minimal influence of NPS in their example, both variants suffer from NPS to the same extent since a Neo-Hookean material model is used and the conclusion in Reference 15 on the relative behavior of the variants remains valid.

4.3 | Three-point bending test with elasto-plastic material model

To demonstrate the relevance of NPS in elasto-plastic problems, a three-point bending test is investigated in the commercial software LS-DYNA. Von-Mises model (LS-DYNA material model no. 24) is used with Young's modulus $E = 217,500$, Poisson's ratio $\nu = 0.3$, yield stress $\sigma_Y = 274$ and a tangent modulus of 100. The dimensions of the problem are shown in Figure 9 in two different projections. The specimen is discretized with a mesh size of 2.

The punch moves 30 in vertical direction, its displacement is prescribed. All tools are modeled as rigid bodies. Figure 10 shows the deformed configuration.

An explicit dynamic simulation is performed with starting time $t = 0$ and termination time $t = 0.055$. The displacement of the punch as a function of time is

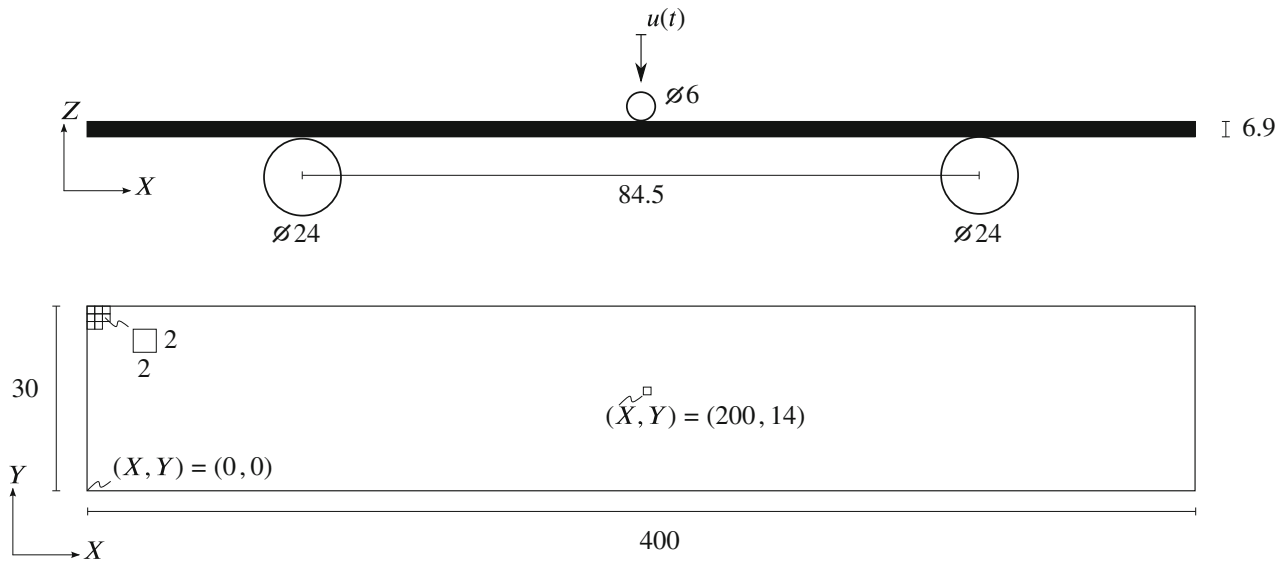$$u(t) = \begin{cases} -3 \cdot 10^4 t^2 & t \leq 0.01 \\ -600(t - 0.01) - 3 & t > 0.01 \end{cases}. \tag{89}$$

FIGURE 9 Three-point bending test: Geometry description in the initial configuration.
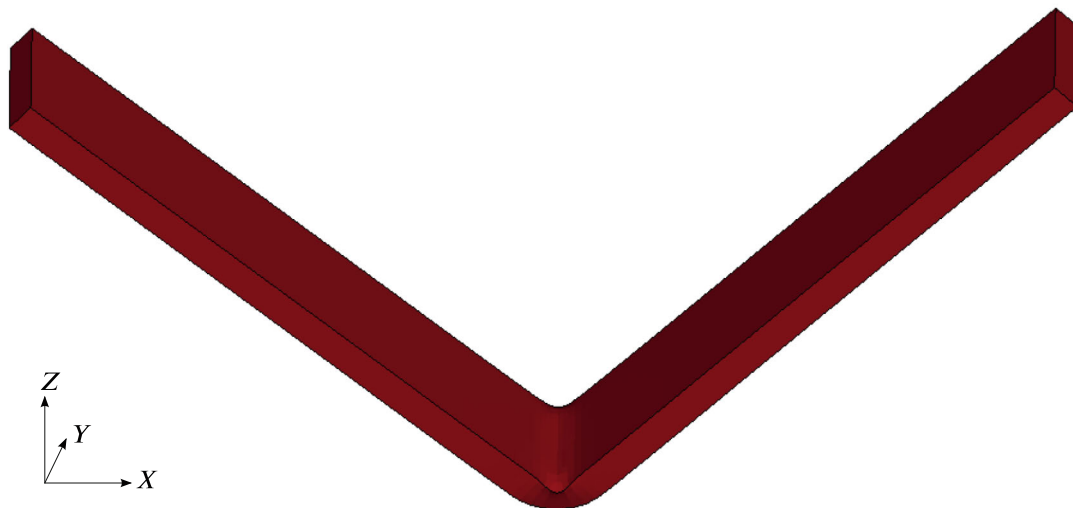

FIGURE 10 Three-point bending test: Deformed geometry.

Three different discretizations are used: the LS-DYNA standard shell element (LS-DYNA shell no. 2), which is an implementation of Reference 23, eight solid elements (LS-DYNA solid element no. 1) across the thickness, and shell element no. 25 in LS-DYNA, which is a 3d-shell element that suffers from NPS, as explained in Section 3.6. All elements use reduced integration. The solid element is integrated with one integration point, both shell no. 2 and 25 are integrated with 9 integration points across the thickness. Figure 11 shows the reaction force of the punch plotted against the punch displacement u.

The force-displacement curve obtained with the standard shell element and the solid discretization agree very well. Starting from approximately $u = 5$, shell no. 25 differs from these solutions and behaves too stiff. The force value at $u = 30$ is about 17% higher compared to the solutions with standard shell elements and solids.

The influence of NPS is even more pronounced in the stress results. Figure 12 (left) plots σ_x over the thickness, evaluated at the element which has its lower left corner at $X = 200$, $Y = 14$ in the initial configuration, see Figure 9. The thickness coordinate is 1 on the upper surface of the specimen and -1 on its lower surface, see Figure 12 (right).
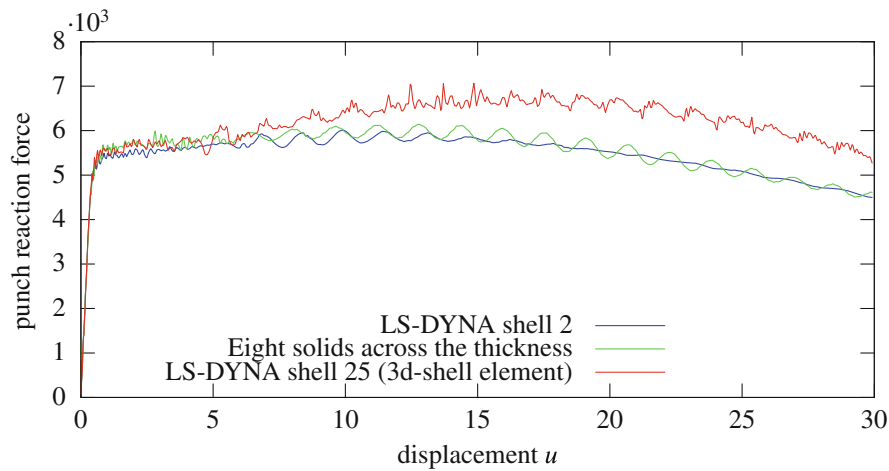
FIGURE 11 Three-point bending test: Force displacement curve for three different discretizations.
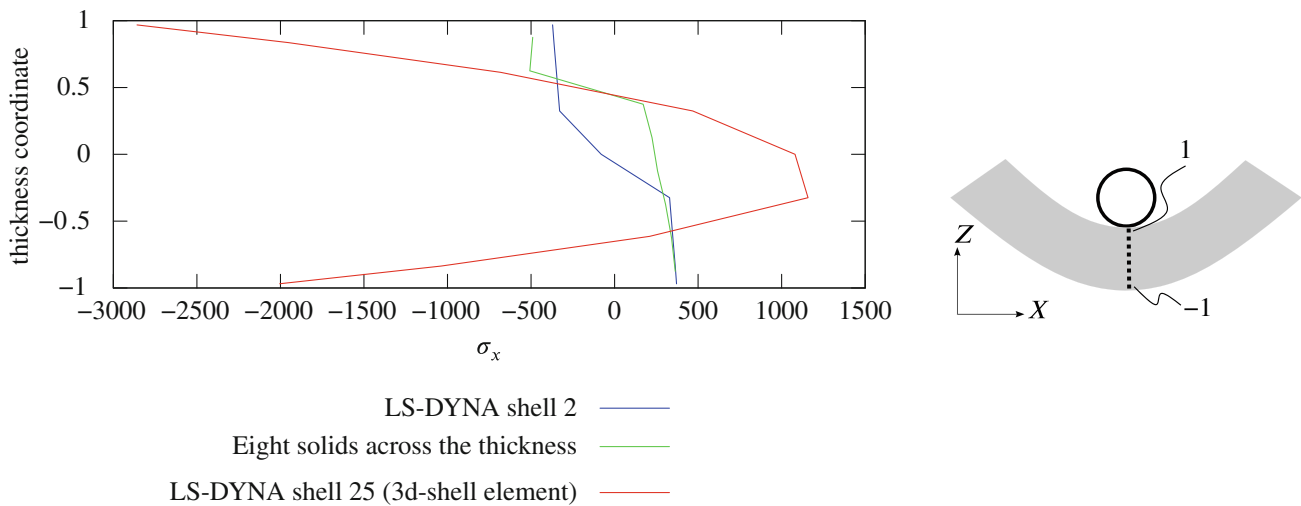

FIGURE 12 Three-point bending test: Stress σ_x plotted against the shell thickness (left) and definition of the thickness coordinate (right).

The parasitic stresses due to NPS dominate the solution of shell element no. 25. The parasitic stresses are quadratic with respect to the thickness, because the leading term in the residual of the isochoric condition is quadratic (see e.g., Equation 37).

5 | CONCLUSION AND OUTLOOK

The study explains the previously unknown effect of *nonlinear Poisson stiffening* (NPS) as a geometrically nonlinear version of an effect that is known as Poisson thickness locking (called linear Poisson stiffening—LPS in this article) in the context of 3d-shell elements. It appears due to the inability of 3d-shell elements to satisfy the isochoric condition in a geometrically nonlinear setup.

Often, 3d-shell elements for geometrically nonlinear problems are based on a 7-parameter shell model and include contributions of the strain tensor that are quadratic with respect to the thickness coordinate ζ. Therefore, they suffer from NPS. In this article, this has been shown for two element formulations from the literature, but the theory explained in this article applies to many other element formulations as well.

Depending on the type of strain energy density function used, nonlinear Poisson stiffening can be prevented in different ways. In case the volumetric part of the strain energy function is a function of the trace of the Green–Lagrange

strain (trE case), adding quadratic normal strain components in thickness direction resolves the issue of nonlinear Poisson stiffening. If the volumetric part is based on the determinant of the deformation gradient (detF case), enhancing the transverse normal strain mitigates the effect of nonlinear Poisson stiffening but cannot fully eliminate it.

Within this article, all enhanced strain components are constant in ξ and η, for example, we added only $L_2(\zeta)$ but not $\xi L_2(\zeta)$, $\eta L_2(\zeta)$, and $\xi \eta L_2(\zeta)$ as enhanced transverse normal strain in the trE case. This was sufficient for the uniaxial bending problems investigated in this article. For more complex deformations, additional mixed enhancements might be beneficial. A detailed analysis of this issue might be an interesting question for further research.

DATA AVAILABILITY STATEMENT
Data sharing is not applicable to this article as no new data were created or analyzed in this study.

ORCID
Tobias Willmann https://orcid.org/0000-0002-0394-6489

REFERENCES

1. Simo JC, Rifai MS. A class of mixed assumed strain methods and the method of incompatible modes. *Int J Numer Methods Eng*. 1990;29(8):1595-1638. doi:10.1002/nme.1620290802
2. Büchter N, Ramm E. 3D-extension of nonlinear shell equations based on the enhanced assumed strain concept. *Comput Methods Appl Sci*. 1992;39-59. https://openlibrary.org/works/OL4300360W/Computational_methods_in_applied_sciences
3. Betsch P, Gruttmann F, Stein E. A 4-node finite shell element for the implementation of general hyperelastic 3D-elasticity at finite strains. *Comput Methods Appl Mech Eng*. 1996;130(1):57-79. http://www.sciencedirect.com/science/article/pii/0045782595009205
4. Sansour C. A theory and finite element formulation of shells at finite deformations involving thickness change: circumventing the use of a rotation tensor. *Arch Appl Mech*. 1995;65(3):194-216. doi:10.1007/BF00799298
5. Parisch H. A continuum-based shell theory for non-linear applications. *Int J Numer Methods Eng*. 1995;38(11):1855-1883. doi:10.1002/nme.1620381105
6. Toscano R, Dvorkin E. A shell element for finite strain analyses: hyperelastic material models. *Eng Comput*. 2007;24(5):514-535. doi:10.1108/02644400710755898
7. Mostafa M, Sivaselvan M, Felippa C. A solid-shell corotational element based on ANDES, ANS and EAS for geometrically nonlinear structural analysis. *Int J Numer Methods Eng*. 2013;95(2):145-180. doi:10.1002/nme.4504
8. Bishara D, Jabareen M. Does the classical solid-shell element with the assumed natural strain method satisfy the three-dimensional patch test for arbitrary geometry? *Finite Elem Anal Des*. 2020;168:103331. doi:10.1016/j.finel.2019.103331
9. Hosseini S, Remmers JJC, Verhoosel CV, de Borst R. An isogeometric solid-like shell element for nonlinear analysis. *Int J Numer Methods Eng*. 2013;95(3):238-256. doi:10.1002/nme.4505
10. Echter R, Oesterle B, Bischoff M. A hierarchic family of isogeometric shell finite elements. *Comput Methods Appl Mech Eng*. 2013;254:170-180. doi:10.1016/j.cma.2012.10.018
11. Choi MJ, Sauer RA, Klinkel S. An isogeometric finite element formulation for geometrically exact Timoshenko beams with extensible directors. *Comput Methods Appl Mech Eng*. 2021;385:113993. doi:10.1016/j.cma.2021.113993
12. Babuška I, Suri M. On locking and robustness in the finite element method. *SIAM J Numer Anal*. 1992;29(5):1261-1293. doi:10.1137/0729075
13. Fleischer M. *Absicherung der virtuellen Prozesskette für Folgeoperationen in der Umformtechnik*. Dissertation. Technische Universität München, München; 2009.
14. Irslinger J. *Mechanische Grundlagen und Numerik dreidimensionaler Schalenelemente*. Dissertation. Universität Stuttgart, Stuttgart; 2013. 10.18419/opus-511
15. Schwarze M, Reese S. A reduced integration solid-shell finite element based on the EAS and the ANS concept-large deformation problems. *Int J Numer Methods Eng*. 2011;85(3):289-329. doi:10.1002/nme.2966
16. Bonet J, Wood RD. *Nonlinear Continuum Mechanics for Finite Element Analysis*. 2nd ed. Cambridge University Press; 2008.
17. de Sousa ARJ, RPR C, Fontes Valente RA, Yoon JW, Grácio JJ, Natal Jorge RM. A new one-point quadrature enhanced assumed strain (EAS) solid-shell element with multiple integration points along thickness - part II: nonlinear applications. *Int J Numer Methods Eng*. 2006;67(2):160-188. doi:10.1002/nme.1609

18. Bathe KJ, Dvorkin EN. A formulation of general shell elements - the use of mixed interpolation of tensorial components. *Int J Numer Methods Eng*. 1986;22(3):697-722. doi:10.1002/nme.1620220312

19. Bischoff M. *Theorie und Numerik einer dreidimensionalen Schalenformulierung*. Dissertation. Universität Stuttgart, Stuttgart; 1999. https://elib.uni-stuttgart.de/handle/11682/143

20. Andelfinger U, Ramm E. EAS-elements for two-dimensional, three-dimensional, plate and shell structures and their equivalence to HR-elements. *Int J Numer Methods Eng*. 1993;36(8):1311-1337. doi:10.1002/nme.1620360805

21. Simo J, Taylor R, Pister K. Variational and projection methods for the volume constraint in finite deformation elasto-plasticity. *Comput Methods Appl Mech Eng*. 1985;51(1):177-208. doi:10.1016/0045-7825(85)90033-7

22. Pian THH, Sumihara K. Rational approach for assumed stress finite elements. *Int J Numer Methods Eng*. 1984;20(9):1685-1695. doi:10.1002/nme.1620200911

23. Belytschko T, Lin JI, Chen-Shyh T. Explicit algorithms for the nonlinear dynamics of shells. *Comput Methods Appl Mech Eng*. 1984;42(2):225-251. doi:10.1016/0045-7825(84)90026-4

24. LS-DYNA theory manual. Livermore Software Technology Corporation (LSTC). r11261 ed; 2019.

25. Butz A, Wessel A, Bischoff M, Willmann T. *Verbesserte Blechumformsimulation durch 3D-Werkstoffmodelle und erweiterte Schalenformulierungen - EFB-Forschungsbericht Nr. 532*. Europäische Forschungsgesellschaft für Blechverarbeitung e.V. (EFB); 2020.

26. Portillo D, del Pozo D, Rodríguez-Galán D, Segurado J, Romero I. MUESLI - a material universal library. *Adv Eng Softw*. 2017;105:1-8. doi:10.1016/j.advengsoft.2017.01.007

27. Barfusz O, van der Velden T, Brepols T, Holthusen H, Reese S. A reduced integration-based solid-shell finite element formulation for gradient-extended damage. *Comput Methods Appl Mech Eng*. 2021;382:113884. doi:10.1016/j.cma.2021.113884

28. Barfusz O, van der Velden T, Brepols T, Reese S. Gradient-extended damage analysis with reduced integration-based solid-shells at large deformations. *Comput Methods Appl Mech Eng*. 2022;389:114317. doi:10.1016/j.cma.2021.114317

29. Büchter N, Ramm E, Roehl D. Three-dimensional extension of non-linear shell formulation based on the enhanced assumed strain concept. *Int J Numer Methods Eng*. 1994;37(15):2551-2568. doi:10.1002/nme.1620371504

APPENDIX A. DERIVATION OF THE ISOCHORIC CONDITION

$$
1 = \det \mathbf{C} = \det(2\mathbf{E} + \mathbf{I}) = \begin{bmatrix} 1 + 2E_{11} & 2E_{12} & 2E_{13} \\ 2E_{21} & 1 + 2E_{22} & 2E_{23} \\ 2E_{31} & 2E_{32} & 1 + 2E_{33} \end{bmatrix}
$$

$$
= (1 + 2E_{11})(1 + 2E_{22})(1 + 2E_{33}) + 8E_{12}E_{23}E_{31} + 8E_{13}E_{21}E_{32}
$$
$$
- 4E_{31}E_{13}(1 + 2E_{22}) - 4E_{32}E_{23}(1 + 2E_{11}) - 4E_{21}E_{12}(1 + 2E_{33}).
$$

The following modifications can be made:

$$
(1 + 2E_{11})(1 + 2E_{22})(1 + 2E_{33}) = (1 + 2E_{11})(1 + 2E_{22}) + 2E_{33}(1 + 2E_{11})(1 + 2E_{22})
$$
$$
4E_{21}E_{12}(1 + 2E_{33}) = 4E_{21}E_{12} + 2E_{33}4E_{21}E_{12}.
$$

Using the symmetry of **E** yields

$$
8E_{12}E_{23}E_{31} + 8E_{13}E_{21}E_{32} = 16E_{12}E_{13}E_{23}
$$
$$
4E_{31}E_{13}(1 + 2E_{22}) = 4E_{13}^2(1 + 2E_{22})
$$
$$
4E_{32}E_{23}(1 + 2E_{11}) = 4E_{23}^2(1 + 2E_{11}).
$$

Inserting these results into the initial equation and sorting for E_{33} yields

$$
1 = 2E_{33}\left[(1 + 2E_{11})(1 + 2E_{22}) - 4E_{21}E_{12}\right] + \left[(1 + 2E_{11})(1 + 2E_{22}) - 4E_{21}E_{12}\right]
$$
$$
- 4E_{13}^2(1 + 2E_{22}) - 4E_{23}^2(1 + 2E_{11}) + 16E_{12}E_{13}E_{23}.
$$

Furthermore, we use the relation

$$M_{3,3}(\mathbf{C}) = (1 + 2E_{11})(1 + 2E_{22}) - 4E_{21}E_{12},$$

resulting in

$$1 = 2E_{33}M_{3,3}(\mathbf{C}) + M_{3,3}(\mathbf{C}) - 4E_{13}^2(1 + 2E_{22}) - 4E_{23}^2(1 + 2E_{11}) + 16E_{12}E_{13}E_{23}.$$

By solving for E_{33} we obtain the final result

$$E_{33} \overset{!}{=} \frac{1 - M_{3,3}(\mathbf{C}) + 4E_{13}^2(1 + 2E_{22}) + 4E_{23}^2(1 + 2E_{11}) - 16E_{12}E_{13}E_{23}}{2M_{3,3}(\mathbf{C})}.$$

Division by $M_{3,3}(\mathbf{C})$ in the last step is a valid operation because we know from Sylvester's criterion that $M_{3,3}(\mathbf{C}) > 0$.

APPENDIX B. CALCULATION OF STRAINS AND ISOCHORIC CONDITION FOR THE GEOMETRICALLY NONLINEAR, LARGE STRAIN CASE

To calculate the strain tensors $\mathbf{E}^1$ and $\mathbf{E}^{\text{red},1}$ for the detF case, we start from the displacement gradient

$$\mathbf{H} = \begin{bmatrix} k_1\zeta & 0 & k_1\xi \\ 0 & 0 & 0 \\ 0 & 0 & k_3 \end{bmatrix}.$$

Evaluation of

$$\mathbf{E}^u = \frac{1}{2}\left(\mathbf{H} + \mathbf{H}^T + \mathbf{H}^T\mathbf{H}\right),$$

yields

$$\mathbf{E}^u = \begin{bmatrix} k_1\zeta + \frac{1}{2}k_1^1\zeta^2 & 0 & \frac{1}{2}k_1\xi + \frac{1}{2}k_1^2\xi\zeta \\ 0 & 0 & 0 \\ \frac{1}{2}k_1\xi + \frac{1}{2}k_1^2\xi\zeta & 0 & k_3 + \frac{1}{2}k_3^2 + \frac{1}{2}k_1^2\xi^2 \end{bmatrix}.$$

By using the definition for c (see (32c))

$$c = k_3 + \frac{1}{2}k_3^2 + \frac{1}{2}k_1^2\xi^2,$$

and adding $\tilde{\mathbf{E}}^1$, the strain tensor becomes

$$\mathbf{E}^1 = \mathbf{E}^u + \tilde{\mathbf{E}}^1 = \begin{bmatrix} k_1\zeta + \frac{1}{2}k_1^1\zeta^2 & 0 & \frac{1}{2}k_1\xi + \frac{1}{2}k_1^2\xi\zeta \\ 0 & 0 & 0 \\ \frac{1}{2}k_1\xi + \frac{1}{2}k_1^2\xi\zeta & 0 & c + \alpha_1\zeta \end{bmatrix}.$$

E_{13} is evaluated at collocation points $A = (0, -1, 0)$ and $B = (0, 1, 0)$ using the ANS method, see Figure 2. Both evaluations yield $E_{13} = E_{31} = 0$ due to $\xi = 0$ at A and B. This yields the final result

$$\mathbf{E}^1 = \begin{bmatrix} k_1\zeta + \frac{1}{2}k_1^1\zeta^2 & 0 & 0 \\ 0 & 0 & 0 \\ 0 & 0 & c + \alpha_1\zeta \end{bmatrix}.$$

$\mathbf{E}^{\text{red},1}$ can be obtained thereof by eliminating the quadratic contributions in ζ, that is, by eliminating $\frac{1}{2}k_1^1\zeta^2$.

Due to $E_{13} = E_{23} = 0$, (10c) simplifies for $\mathbf{E}^1$ and $\mathbf{E}^{\text{red},1}$ to

$$E_{33} \overset{!}{=} \frac{1 - M_{3,3}(\mathbf{C})}{2M_{3,3}(\mathbf{C})}.$$

With

$$M_{3,3}(\mathbf{C}) = 1 + 2E_{11},$$

where E_{11} is taken from $\mathbf{E}^1$ and $\mathbf{E}^{\text{red},1}$ respectively, this can be written as

$$E_{33} \overset{!}{=} -\frac{2E_{11}}{2 + 4E_{11}},$$

which is the result in (47) and (46).